Airframe Noise Simulations of a Full-Scale Large Civil Transport in Landing Configuration

Mehdi R. Khorrami[1],
NASA Langley Research Center, Hampton, VA, 23681, USA

Benedikt König,[2] Ehab Fares,[3] André F.P. Ribeiro,[2]
Dassault Systèmes Deutschland GmbH, D-70563, Stuttgart, Germany

Michael Czech,[4]
The Boeing Company, Mukilteo, WA, 98275, USA

and
Patricio A. Ravetta[5]
AVEC Inc., Blacksburg, VA, 24060, USA

This paper summarizes the results obtained from an extensive computational campaign to accurately predict full-scale landing gear noise for large civil transports. A highly accurate digital model of a full-scale Boeing 777-300ER aircraft with as-flown nose and main landing gear components was developed for use in the simulations. Two aircraft configurations were selected: nose and main landing gear deployed with wing high-lift devices retracted, and nose and main landing gear deployed with wing high-lift devices deflected. The two configurations were simulated without and with toboggan fairings installed on the main gear to represent the principal configurations evaluated during the 2005 QTD2 flight test. All simulations were performed with the lattice Boltzmann solver PowerFLOW® to resolve and capture the highly complex, unsteady flow field in the immediate vicinity of the aircraft. The far-field noise signature of the aircraft was computed via a Ffowcs-Williams and Hawkings integral approach, with flow quantities on a permeable surface enclosing the source regions used as input. Synthetic pressure records at ground array microphone locations used during the QDT2 test were employed to generate narrowband acoustic maps and integrated far-field noise spectra. With high-lift devices retracted, the predicted spectra showed that landing gear noise is equivalent to total airframe noise, with no other airframe sources appearing within 10 dB of gear peak levels. Application of a toboggan fairing to the main gear produced modest noise reductions of 1-2 dB across the resolved frequency range. With high-lift devices deflected, undercarriage noise was within 3-4 dB of the total airframe noise, thus comprising nearly half of the total airframe noise. For this configuration, the toboggan fairing did not produce a reduction in noise, corroborating trends previously observed in QTD2 flight test data.

---

[1] Senior Scientist, Computational AeroSciences Branch, Associate Fellow AIAA.

[2] Senior Specialist, SIMULIA Aerospace & Defense.

[3] Director, Aerospace and Defense (currently with Geely Auto Technical, Deutschland, GmbH), Senior Member AIAA.

[4] Acoustics Engineer, Member AIAA.

[5] Co-owner, Chief Research Engineer, Senior Member AIAA.

I. Introduction

Airframe noise contributes significantly to the total noise generated by modern aircraft during approach and landing. The primary sources of airframe noise are the aircraft undercarriage and wing high-lift devices (slats and flaps) [1]. For large, twin-aisle civil airliners, contributions from the landing gear to the total airframe noise signature increase substantially [2-4]. Simulation-based prediction of airframe noise is an important tool for the design of effective noise-reduction strategies that can substantially improve the quality of life in communities near major airports. Physically accurate prediction of airframe noise for a full-scale, large airliner with high-lift devices and undercarriage deployed is a grand challenge for the aerospace community. For these aircraft, the extreme geometrical complexity of the airframe components deployed during landing generates noise-producing flow features that contain a broad range of spatio-temporal scales. Such simulations were deemed unattainable just a few years ago. The study summarized here is part of a larger effort, the first of its kind, toward meeting this grand challenge.

Leveraging the advances and insights gained under the NASA Environmentally Responsible Aviation and Flight Demonstrations and Capabilities projects, the NASA-Boeing joint effort on airframe noise prediction was initiated to extend simulation-based methodology to the undercarriage and high-lift systems of full-scale, large civil transports. Started in the fall of 2015 and spanning nearly five years, the effort was executed in a succession of steps whereby the complexity and relevance of the studied configuration to the full-scale, complete aircraft were gradually increased. A Boeing 777 aircraft was selected as the testbed geometry due to availability of model- and full-scale experimental data for validation purposes.

As a first step, the simulations targeted a 26%-scale, high-fidelity B777-200 main landing gear (MLG) model in isolation. This proof-of-concept effort determined that the computations were able to capture the far-field noise footprint and other appropriate trends for an isolated, model-scale MLG. These simulations produced results [5-6] that were in excellent agreement with wind-tunnel acoustic measurements [7]. These simulations were also instrumental in demonstrating clearly that only flow variables computed on a permeable data surface could be used as input to a Ffowcs-Williams and Hawkings (FWH) integral method [8] to produce the correct far-field noise spectrum. That is, the less computationally intensive approach of using the computed fluctuating pressure field on the model solid surface as input to the FWH method significantly overpredicted the sound pressure levels (SPL). Therefore, the computational cost for all subsequent configurations was substantially increased, since the high-resolution region in the immediate vicinity of the model had to be extended to the permeable data surface.

Simulations of the 26%-scale, semispan B777-200 (also referred to as Subsonic Transport Aeroacoustic Research or STAR) model with main gear, slats, and flaps deployed (landing configuration) were undertaken in the next phase. This configuration enabled us to examine the accuracy of the predicted aeroacoustic data for an installed MLG and to validate the computations against available experimental measurements of the STAR model [9-11]. The simulation campaign targeting the semispan STAR model and validation of the simulated results is discussed in references [12] and [13].

Simulations of the full-scale, installed nose landing gear (NLG) of a B777-300ER aircraft in combination with a cruise wing were performed in the third phase [14]. We had determined previously [15] that the forward location of the NLG, away from other airframe components, precluded interactions among the noise produced by this component and those of the main gear and high-lift devices. As a result, the setup for the practically isolated NLG enabled simulations at a very fine spatial resolution that would have been prohibitive if the MLG were also deployed. By performing the NLG simulations at successively finer resolutions, we were able to ascertain the full effect of spatial resolution on predicted sound levels and frequency content of the far-field spectrum. This approach also helped us develop a meshing strategy better suited for the extremely challenging case of the aircraft in a landing configuration. The computational effort on the full-scale NLG is described in Ref. [14].

The present paper discusses the fourth and last phase of the NASA-Boeing joint effort, which targeted the most challenging configurations: full-scale, complete B777-300ER aircraft with NLG and MLG deployed and wing high-lift devices either stowed or deflected. Here, we present and analyze the computational results. Validation of the predicted noise signatures produced by the NLG and MLG with microphone array measurements from flight tests of the same aircraft [4] are provided in Ref. [16].

II. Simulated Geometries and Flight Conditions

An abbreviated account of the geometries that were developed in support of the fourth phase of the NASA-Boeing effort on airframe noise is provided in this section, followed by a short description of the flight conditions that were used during the present simulations.

A. Digital Model of the Full-Scale Aircraft

The digital model of a full-scale, full-span B777-300ER was painstakingly developed in stages over a period of three years by Geometry Laboratory (GeoLab) personnel at the NASA Langley Research Center. The fuselage and most of the wing (including high-lift devices) were generated by scaling up the 26%-scale 777-200 (STAR) model. Geometry definitions for two fuselage extension plugs, horizontal and vertical tails, and wing outboard segments delivered by Boeing were used to convert the aircraft to a -300ER version. Since the main focus of the NASA-Boeing collaboration was landing gear noise, most of the effort and resources were spent developing a CFD-ready, CAD definition of the undercarriage system. A geometry for the NLG was developed first to support the third phase of the NASA-Boeing collaboration [14]. Substantial effort was spent on converting the full-scale CAD geometry (including the NLG bay) provided by Boeing into a CFD-ready, digital representation of the physical nose gear. Through multiple iterations that lasted a few months, several geometry discrepancies involving the finer features of the NLG were identified and remedied. After a digital model of the NLG was created, attention was redirected toward the development of a full-scale B777-300ER MLG. Starting with the Boeing-delivered CAD geometry, a process similar to that executed for the NLG was followed. However, the extreme complexities of the MLG and its wheel bay necessitated a much longer development period. Extreme care was exercised during this crucial phase to ensure that the digital NLG and MLG models faithfully replicated the full-scale landing gear as currently flown on B777-300ER aircraft. A realistic rendering of the digital model of the B777-300ER in landing configuration is presented in Fig. 1a.

For the present simulations, the two baseline aircraft configurations of interest were a) NLG and MLG deployed with wing high-lift devices retracted (Config1); and b) NLG, MLG, and wing high-lift devices deployed (Config2); as shown in Figs. 1b and 1c, respectively. Close-up images of the CAD model developed for the full-scale nose and main landing gears are displayed in Figs. 2a and 2b, respectively. The configuration with the toboggan fairing installed on the MLG is shown in Fig. 2c.

a) Far and close-up view of rendered full-scale digital model in landing configuration

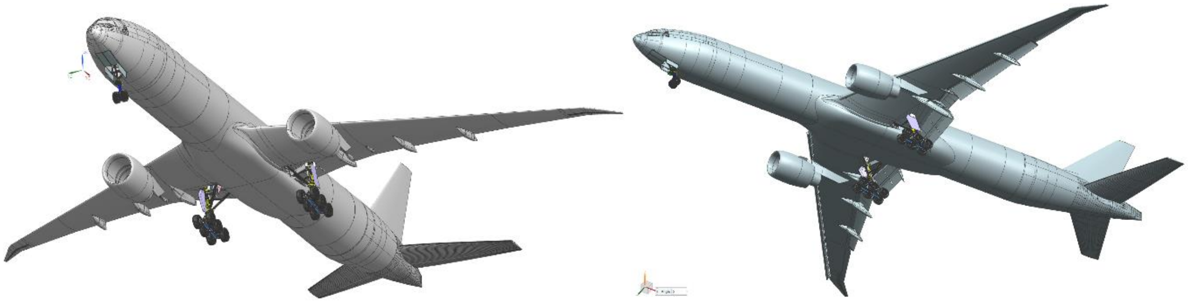

b) High-lift devices retracted (Config1) **c) High-lift devices deflected (Config2)**

Fig. 1 Full-scale B777-300ER aircraft with NLG and MLG deployed.

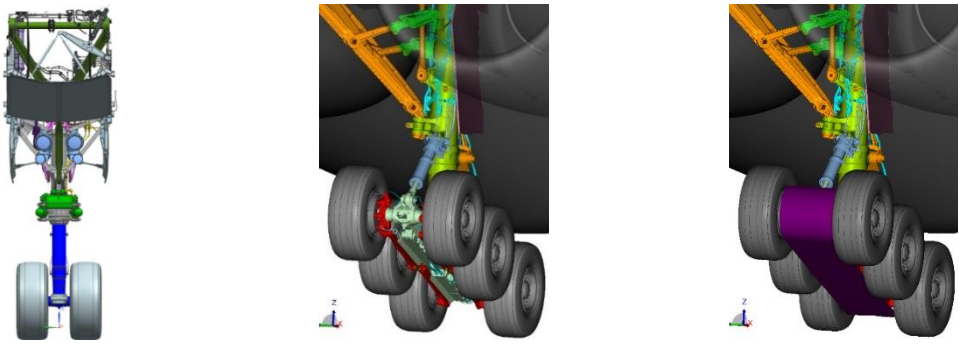

a) Nose landing gear **b) Baseline main landing gear** **c) Main gear with toboggan**

Fig. 2 Close-up view of modeled full-scale B777-300ER landing gears.

B. Simulated Flight Conditions

With the exception of Reynolds number (Re), the simulations were performed at flight conditions and aircraft parameters that matched those recorded during two passes over the array of the selected aircraft configurations, performed during the 2005 Quiet Technology Demonstrator II (QTD2) test [4]. The flight conditions for the case of landing gear deployed with cruise wing (Config1) and landing gear and high-lift devices deployed (Config2) are listed in Table 1. The Re for all computations was 20×10^6, which is approximately 50% of the flight Re based on mean aerodynamic chord and aircraft landing speed for Config2 and approximately 35% for Config1. This Re is sufficiently high to produce far-field noise levels that are nearly equivalent, at a lower computational cost, to those obtained at full flight Re [17, 18]. A schematic of aircraft orientation relative to the microphone array on the ground is depicted in Fig. 3.

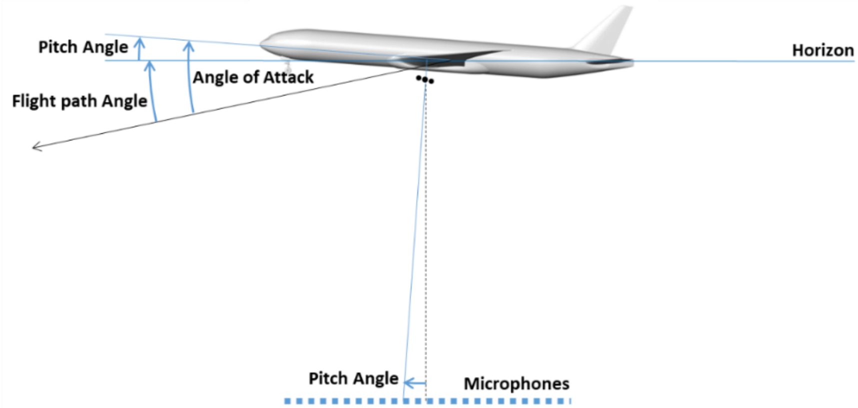

Fig. 3 Schematic of aircraft orientation relative to the microphone array on the ground (from Ref. [14]).

Table 1. Flight conditions used for simulations of selected aircraft configurations.

Configuration	Angle of Attack (AoA)	M	Speed (kts)	Re
Config1	6.5°	0.344	229.8	20×10^6
Config2	4.0°	0.254	168.9	20×10^6

III. Computational Approach

The computational methodology employed in this study is identical to that described in Refs. [12, 14]. All simulations were performed with the Dassault Systèmes PowerFLOW® solver based on the lattice Boltzmann method (LBM). Full descriptions of the solver, turbulence modeling, wall boundary treatment, and far-field sound propagation method used are given in Ref. [14]. Here, we present aspects of the computational effort that were pertinent to the simulations discussed in this study.

A. Computational Grids

The computational grids constructed for Config1 and Config2 borrowed elements from various model- and full-scale grids developed during the previous phases of the NASA-Boeing collaboration. The grid for Config1 was generated by integrating the installed NLG grid of Ref. [14] with the 26%-scale isolated MLG grid of Ref. [5] that was resized to full-scale and adapted to accommodate the B777-300ER MLG and its wheel bay. To maintain a manageable grid size during full aircraft computations, the near-wall mesh size for the NLG was slightly relaxed relative to that used in Ref. [14], resulting in a slight degradation in resolution of high frequency sound. As mentioned in section I, the NLG setup of Ref. [14] enabled simulations at several successively finer resolution levels. The corresponding grids were called "xcoarse" (extra-coarse), "coarse", "medium", and "fine". For consistency, we have followed the same naming convention while being fully aware that execution of full-scale, complete aircraft simulations is a massive, extremely challenging undertaking even at what we consider medium spatial resolutions. For reference, we note here that our xcoarse grid provides much better spatial resolution than that used in most other published works.

Starting with the Config1 mesh, the grid for Config2 was constructed by scaling up, adapting, and integrating the grid for the 26%-scale STAR model in landing configuration used in Ref. [12]. Accordingly, the xcoarse and coarse resolution grids for Config2 possess identical spatial resolution for the NLG and MLG components as their Config1 counterpart. For reasons that will be highlighted in section III.B, the spatial resolution for the 'medium' Config2 grid had to be relaxed relative to that used in Config1. Based on the isolated NLG results of Ref. [14], at directivity angles close to overhead, the xcoarse, coarse, medium, and fine grids produced far-field noise spectra that were converged up to frequencies of 1,600 Hz, 2,400 Hz, 3,600 Hz, and 4,800 Hz, respectively. Certainly, we do not expect a similar convergence behavior from the present grids, which encompass a complete aircraft in landing configuration. In fact, with the addition of the MLG, we anticipate a noticeable reduction in the upper bound of the frequency range where the computed solution from each resolution level is deemed to be reasonably converged. Sample images of mesh distribution obtained from several planar cuts of the Config2 xcoarse grid, coarsened by a factor of 2 for clearer visualization, are shown in Fig. 4. The image in Fig. 4a, representing the aircraft symmetry plane, provides a global view of the massive volume mesh surrounding the aircraft where adequate spatial resolution had to be maintained. Notice that the highly-resolved volume does not contain the rear section of the aircraft. This omission was necessary to keep the grid size manageable and the simulations affordable. Since neither primary nor secondary airframe sources are expected to originate from the empennage, any adverse effects from truncating the high-resolution volume would be minimal. A close-up view of the mesh resolution in planes bisecting the NLG and MLG components are shown in Figs. 4b and 4c, respectively. Even at xcoarse resolution levels, most of the small features in the nose and main gears are being resolved with several cells.

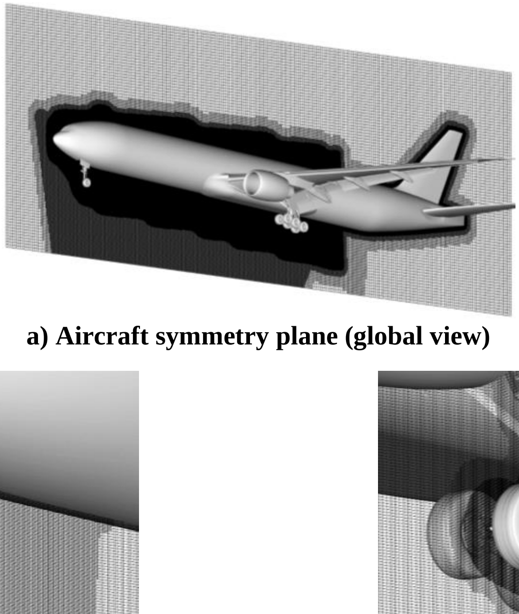
a) Aircraft symmetry plane (global view)

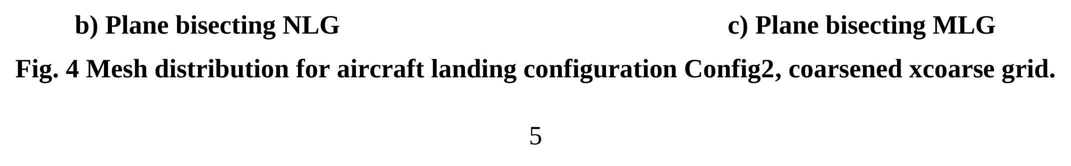
b) Plane bisecting NLG **c) Plane bisecting MLG**

Fig. 4 Mesh distribution for aircraft landing configuration Config2, coarsened xcoarse grid.

An overview of the mesh properties for all configurations and resolutions used in this study is given in Table 2. The Cartesian mesh structure used by PowerFLOW allows for local refinements with a 2-to-1 ratio between cells with different resolution levels. With all simulation setups using consistent local refinement definitions where possible, the minimum cell size provided was sufficient to describe the overall resolution characteristics of each case. Note from Table 2 that the finest voxel edge length – used to resolve the smallest geometrical structures – was reduced by a factor of 1/1.5 between resolution levels, except for the intermediate coarse/medium grid. Explicitly coupled to this spatial resolution is the physical timestep size, leading to an increased number of timesteps, by a factor of 1.5, for identical physical times simulated. For reference, also listed in Table 2 are the total volume and surface elements for each simulation and overall computational costs, illustrating the massive scale of the simulations. Since the effort spanned several years, the stated CPUh reflects the various processors used (mostly Ivy Bridge, with some Haswell and Broadwell).

Table 2. Simulation case sizes for Config1 and Config2 (baseline MLG configuration).

Full-scale NLG + MLG	Resolution					
	Extra coarse		**Coarse**		**Coarse/ Medium**	**Medium**
Reynolds Number	20 x 10^6		20 x 10^6		20 x 10^6	20 x 10^6
Minimum cell size [mm]	1.4		0.94		0.76	0.62
Timesteps (for 2.5s) [10^6]	1.06		1.59		1.94	2.38
Geometry	**Cruise**	**High-lift**	**Cruise**	**High-lift**	**High-lift**	**Cruise**
Volume elements, Voxels [10^6]	2553	5030	7324	14100	25110	23758
Surface elements, Surfels [10^6]	119	188	195	317	427	347
CPUh [1k]	255	1160	669	2921	3900	3700

B. Far-field Noise Propagation

As indicated in section I, our studies of the isolated 26%-scale, high-fidelity B777-200 MLG model [5-7] demonstrated clearly that, for correct prediction of the far-field noise signature, one must rely on a permeable (porous) data surface for input to a FWH integral method [8]. This choice was further confirmed by the NLG study of Ref. [14] and by the extensive work of Spalart et al. [19], where multiple, simpler test configurations were considered. The determination of proper extent, location, and shape of the permeable surface can be a time-consuming process, in particular for extremely complex geometries such as the complete aircraft considered here. Significant effort was devoted to experimentation with the shape and extent of the porous surface. The aim was to construct a surface that a) contained all flow fluctuations produced by the NLG, MLG, and wing, b) resided sufficiently far from the aircraft surface to encompass most of the flow-acoustic interaction region, and c) minimized the enclosed volume (grid size) to ensure that simulations were affordable. Preliminary xcoarse simulations for Config1 and Config2 were used to determine the isosurface of 1% standard deviation of velocity magnitude fluctuations. A penetrable data surface that encompassed this isosurface and resided sufficiently outward from it was determined for each configuration. Our initial goal of devising a permeable surface that would enclose the entire aircraft, including part of the downstream wake, was impractical for spatial resolutions beyond xcoarse since the resulting grid size would have rendered simulations at coarse and medium resolution levels prohibitively expensive. Given the absence of any airframe noise sources in the empennage region, the permeable surface was truncated in a manner that excluded this portion of the aircraft. Computed far-field noise spectra (based on xcoarse simulations) obtained from the full and truncated permeable data surfaces were similar within the range of directivity angles of interest, thus justifying the imposed modification. Accordingly, all the far-field noise spectra presented in this paper were generated from the truncated permeable data surfaces shown in Fig. 5. To accommodate the larger wake generated by the high-lift wing (Config2), notice that the permeable surface for this configuration was expanded to contain additional volume below the aircraft. Because of the extra number of voxels required to define the leading edge slats, trailing edge flaps, and the expanded volume of the permeable surface, the spatial resolution for the Config2 medium grid was relaxed relative to that used for Config1 to obtain a grid of manageable size, as shown in Table 2. We refer to this Config2 grid as “coarse-medium” to distinguish the reduction in resolution. Also notice in Fig. 5 the presence of multiple end caps at the downstream exit plane of the permeable surfaces. These caps were used for data averaging purposes and to ascertain the impact of hydrodynamic fluctuations passing through the downstream plane. Despite our best effort, unfortunately the Config2 expanded permeable surface was too costly for use at resolutions higher than xcoarse. Therefore, the permeable surface devised for Config1 (red line contours in Fig. 5) was used as the primary (nominal) data surface for both configurations. Predicted acoustic results for Config2 obtained with the expanded permeable surface (blue line contours in Fig. 5) from xcoarse simulations were leveraged to determine the effects of data surface proximity to the aircraft body.

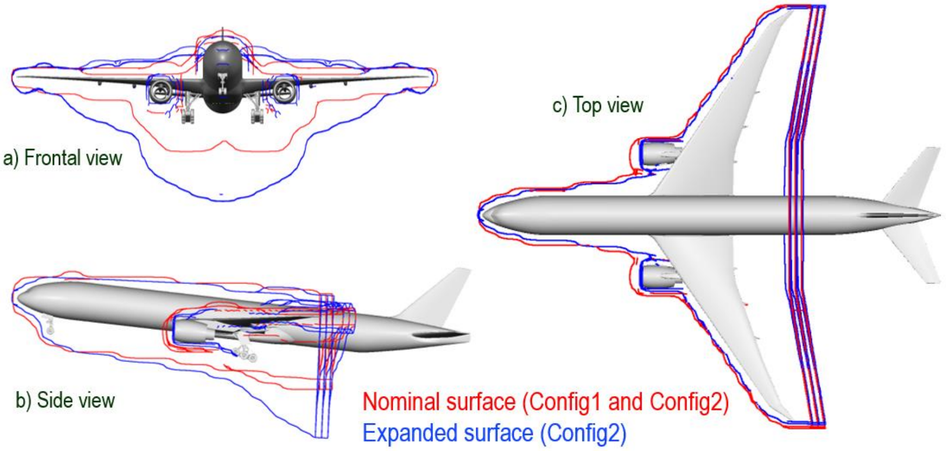

Fig. 5 Permeable data surfaces for Config1 (nominal, red line) and Config2 (blue line) used for far-field noise computations.

To enable direct comparisons with flight test data, synthetic far-field pressure records at the QTD2 array microphone locations on the ground were computed via a FWH integral approach [8] with flow quantities on a permeable data surface used as input. A bottom view of the QTD2 phased microphone array and the aircraft relative position for the Config1 and Config2 aircraft passes are shown in Fig. 6. Notice that the aircraft path was slightly off the array center during these passes. Accounting for convection effects, the aircraft were located in the figures at approximately 90° emission angle relative to the center of the QTD2 flight test array. A total of 1.0 s of data were collected on the permeable surface; of that, approximately 0.2 s were required for data synchronization. Thus, the synthetic microphone array pressure records contain approximately 0.8 s of simulated physical time.

a) Config1 **b) Config2**

Fig. 6 Schematic of QTD2 phased microphone array and relative location of aircraft used in the simulations.

C. Synthetic Array Data Processing

Synthetic microphone pressure records generated from the simulations were processed with the AVEC Phased Array software suite [20] in the manner described in Refs. [18, 21]. Since the simulated data were obtained with the aircraft in a stationary location relative to the array, beamforming in the frequency domain was used. Flow convection effects were included to match flight test conditions (i.e., relative directivity angle). Diagonal removal and array shading were used to improve the results [22]. Beamforming output was post-processed using the CLEAN technique [23], available in the same software suite.

Although array resolution in the direction normal to the array is poor, the relatively large difference in height between the NLG and MLG trucks and the wing high-lift devices may preclude using a single scanning plane to contain and represent all the noise sources. To assess the effect of this height differential, two planar grids named

"Wing" and "Gear", shown in Fig. 7 for the configuration with high-lift devices deflected (Config2), were used to generate beamform maps that provide the position and power spectral density (PSD) of the acoustic sources. The two planes are 2 m (6.56 ft) apart in the direction normal to the scanning planes. The Wing plane, located close to the wing undersurface and depicted in Fig. 8, provided a slightly more accurate representation of the strength and position of the sources associated with the slats and flaps. The Gear plane, shown in Fig. 9, cuts the vertical posts of the NLG and MLG near the mid-section, thus providing similar resolution to the upper and lower gear sources. For Config1, since the high-lift devices are retracted, the Gear plane is sufficient and more appropriate to resolve the relevant sources. For Config2, except at very few frequencies, the two planes produced similar maps with source strength differences less than 0.2 dB. Therefore, unless stated otherwise, all acoustic results presented here were based on the Gear plane.

Beamform and CLEAN maps were generated on a rectangular, 60-m long by 66-m wide planar grid covering most of the aircraft (tail section excluded), as shown in Figs. 8a and 9a. A resolution of 0.3 m was used, resulting in a grid with 201 by 221 points. The planar grid was rotated to match the aircraft angle of attack of each configuration.

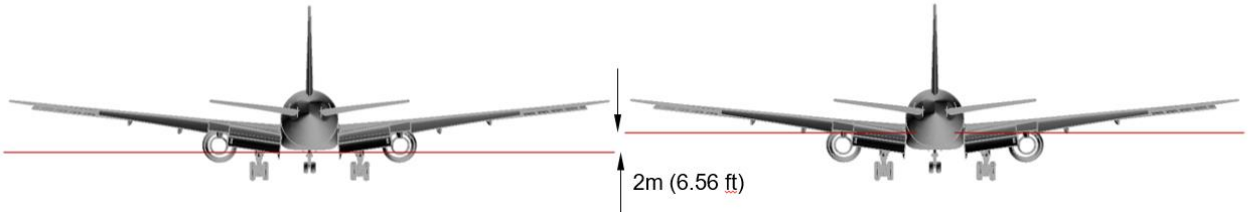

a) Gear plane **b) Wing plane**

Fig. 7 Position and relative distance between scanning planes with aircraft in Config2.

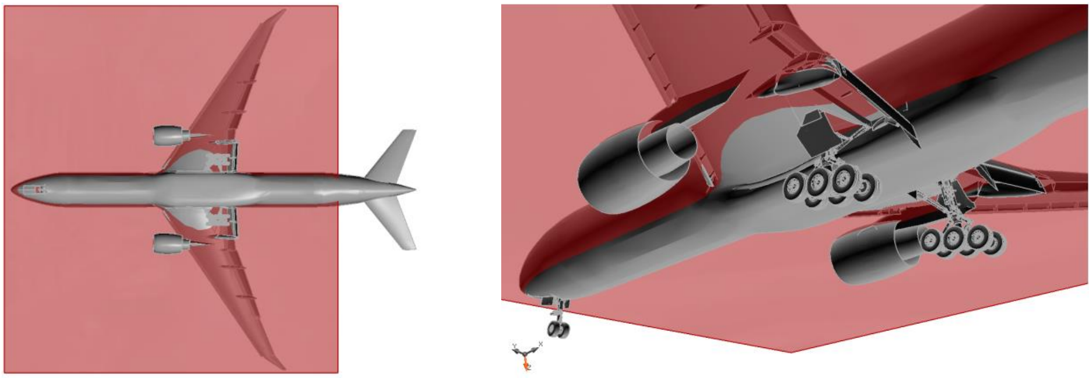

a) Bottom view of full plane **b) Close-up view of landing gear**

Fig. 8 Extent and position of the "Wing" beamforming plane. Grid resolution: 0.3m.

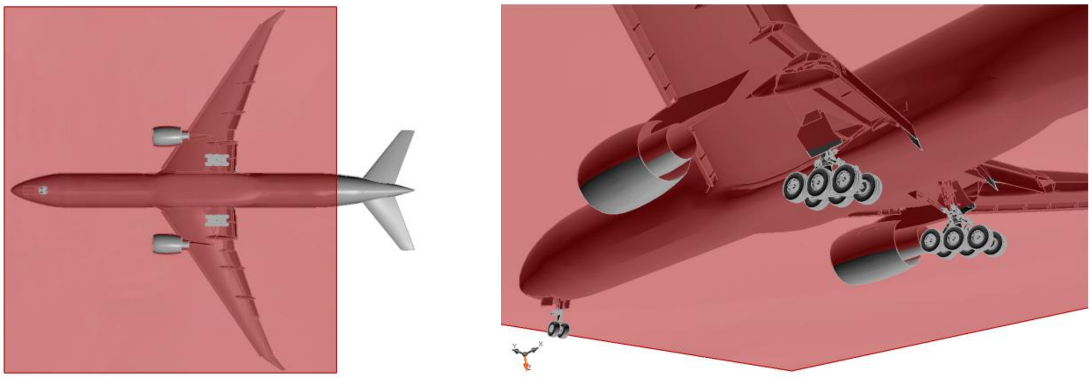

a) Bottom view of full plane **b) Close-up view of landing gear**

Fig. 9 Extent and position of the "Gear" beamforming plane. Grid resolution: 0.3m.

To generate far-field spectra, the CLEAN beamform maps were integrated with a 10 dB cutoff applied. Tailored integration regions were used to determine contributions from various sections of the aircraft. These integration regions are shown in Fig. 10a. Since landing gear noise prediction was the main focus of the NASA-Boeing joint effort, special attention was paid to devise integration regions for the undercarriage components that would enable the contributions and far-field noise signature associated with NLG and MLG to be assessed accurately. A close-up view of the two regions covering the port and starboard MLG are shown in Fig. 10b. For Config1, where high-lift devices are stowed (cruise wing), the full extent of the MLG regions was used in the integration. For Config2, however, the inboard tip of the wing inboard flap adjacent to the fuselage was predicted as a major noise source. As result, to determine the MLG true far-field noise signature, integrated levels from the sub-regions “IB Flap” were subtracted from the corresponding levels obtained for the full MLG regions. The integrated spectrum for the “Whole” grid covering the entire scanning plane was also computed with a 15 dB cutoff to include the contributions from all relevant sources to the overall noise signature. When deconvolving beamform maps with the CLEAN algorithm, sources are often reduced to a single or a few grid cells with non-zero levels, thus impairing visualization. Therefore, CLEAN with an artificial resolution of 0.5 m was also used to obtain maps with easily identifiable sources. Maps generated with a resolution parameter equal to zero were used to obtain more accurate integrated spectral values by avoiding such normalizations.

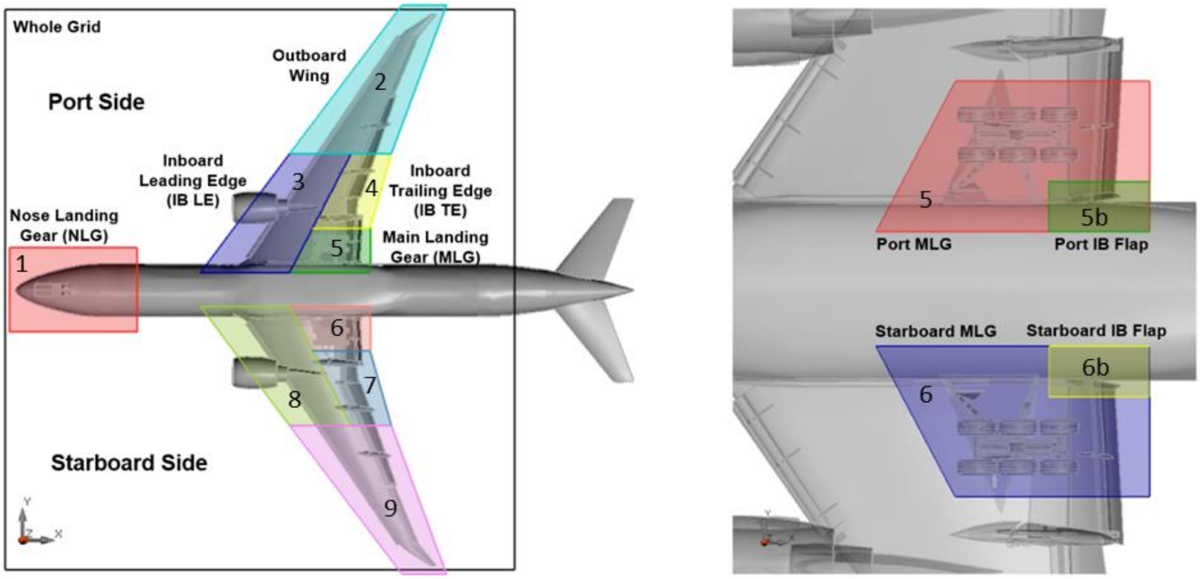

a) Full aircraft **b) Close-up view of MLG and inboard flap tip regions**

Fig. 10 Regions used to calculate NLG and MLG integrated far-field noise spectra.

IV. Results and Discussion

Computational simulations of configurations with extreme geometric complexities are fraught with technical issues and difficulties. A particularly challenging issue pertains to the presence of many small cavities, openings, and gaps in the aircraft undercarriage and high-lift system (e.g., slat or flap brackets). Such openings may produce high-amplitude tonal features (resonance) that could be physical (real) or numerical (spurious), the latter caused mostly by spatial under-resolution of these openings. In most instances, conducting the simulations on successively finer grids causes those resonances that are physical to converge and those that are numerical to significantly subside or disappear altogether [24][6]. Obviously, for large and complex configurations such as those under consideration here, increasing spatial resolution is a costly option that cannot be exercised easily.

As mentioned in section III.A, the naming convention we used to identify grid resolution is consistent with that employed for the NLG simulations of Ref. [14]. For the present study, extra-coarse (xcoarse) and coarse resolution simulations for both Config1 and Config2 without and with toboggan fairings were successfully completed and the

---

[6] In addition to Fig. 42 of Ref. [24], this behavior is clearly seen in the data presented in Figs. 30a and 35a of this paper.

results analyzed. Note from Table 2 that the grids for these simulations are massively large – our xcoarse grid provides much better spatial resolution than that used in most other published works.

Medium and coarse-medium spatial resolution simulations were also performed for Config1 and Config2, respectively. These flow field solutions contained high-amplitude resonances and their harmonics that contaminated the results, both aerodynamic and acoustic, and were not observed at lower resolutions. Closer examination of the fluctuating surface pressure fields revealed that these flow resonances – which originated from the MLG, particularly the starboard main gear – produced tones that were clearly numerical and significantly larger than the broadband component of the unsteady pressure signals. Unfortunately, the sheer size of the medium resolution grids precluded using finer resolution meshes to determine whether these flow resonances were physical or due to under-resolution of some of the smaller gaps and cavities in the MLG geometry. Diagnostic efforts, such as elimination of some smaller openings in the MLG geometry, were deemed futile because the large number of such openings would require multiple simulations at medium-resolution that could not be accommodated within the resources and duration of the NASA-Boeing collaboration. The spurious tones observed in the medium and coarse-medium simulations may have also resulted from unexpected numerical behavior of the solution when the number of voxels in the computational mesh is extremely large. Note from Table 2 that these grids contain 23-25 billion voxels and, as such, are the largest ever used with PowerFLOW. This issue is being investigated by the code developers. Therefore, only results obtained from xcoarse and coarse resolution simulations are included in this paper.

The results presented here are organized as follows. After a brief discussion of the global flow field, computed trends of the integrated aerodynamic forces and time-averaged surface pressure coefficients are presented. Sample source localization (beamform) maps from CLEAN, highlighting the prominent airframe sources and their relative strengths, are discussed next. Followed by the main thrust of this paper: presentation of the integrated far field spectra. Since the NASA-Boeing joint effort focused on landing gear, the discussions mostly target noise signatures associated with the NLG and MLG components. Finally, we conclude with a brief analysis of the velocity scaling laws for the far-field spectral levels produced by the landing gear.

A. Global Flow Field

An instantaneous view of the flow field surrounding the full-scale B777-300ER aircraft in landing configuration (Config2), obtained from coarse resolution simulations, is given in Fig. 11, where resolved vortical structures are shown as isosurfaces of the λ_2 criterion. As anticipated, even at coarse resolution, the unsteady simulation resolves a large spectrum of turbulent structures generated as the flow moves past the NLG, MLG, and wing high-lift devices. Since adequate mesh resolution was maintained downstream of the gear, turbulent wake structures were convected with the local flow and sustained over long distances. Notice that, despite its lateral growth downstream, the NLG wake does not interact with the MLG and passes between the two main gears. Conversely, there is significant interaction between the MLG wakes and the flaps in the inboard section of the wings. The corresponding instantaneous fluctuating pressure field on the aircraft surface is presented in Fig. 12. The images clearly highlight regions of high-amplitude pressure fluctuations associated with imprints of the landing gear on the fuselage and bottom surface of the wings. Snapshots of the fluctuating pressure field emanating from the undercarriage and propagating toward the ground are given in Fig. 13. Figure 13a samples the field for Config1 on two planar cuts containing the NLG and MLG, whereas Fig. 13b depicts the data for Config2 on a plane across the MLG. The images clearly show the extent of the volume enclosed by the permeable surface: the radiating pressure field under the aircraft is finely resolved to maintain phase and amplitude content until the waves reach the surface where flow data are collected.

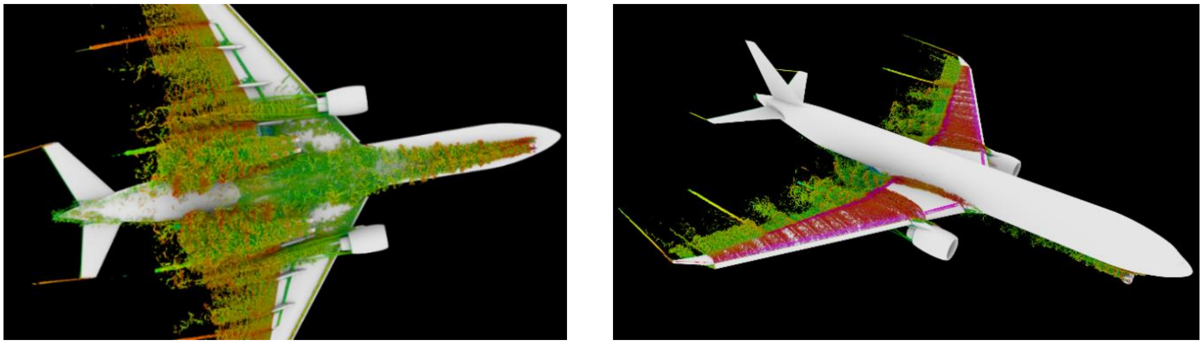

a) Bottom view **b) Top view**

Fig. 11 Instantaneous vorticity field based on isosurfaces of λ_2 criterion for full-scale B777-300ER with landing gear and high-lift devices deployed (landing configuration, Config2).

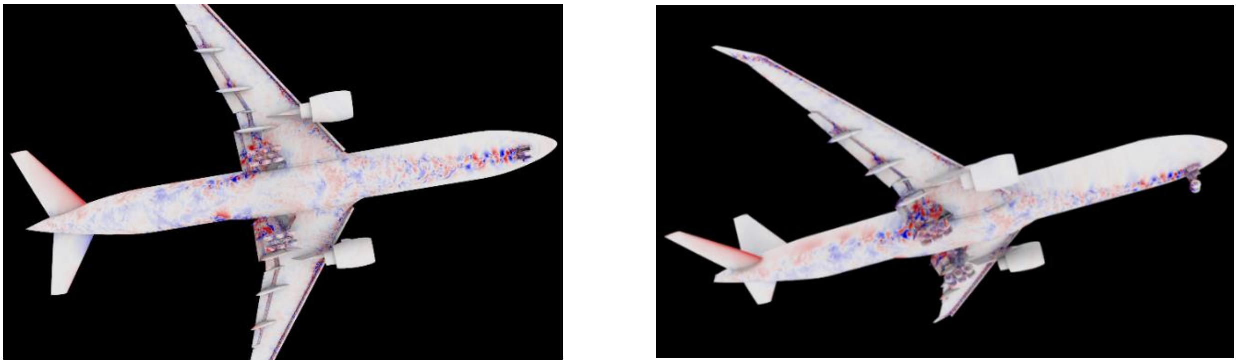

a) Bottom view b) Side view

Fig. 12 Instantaneous fluctuating surface pressure field for full-scale B777-300ER with landing gear and high-lift devices deployed (landing configuration, Config2).

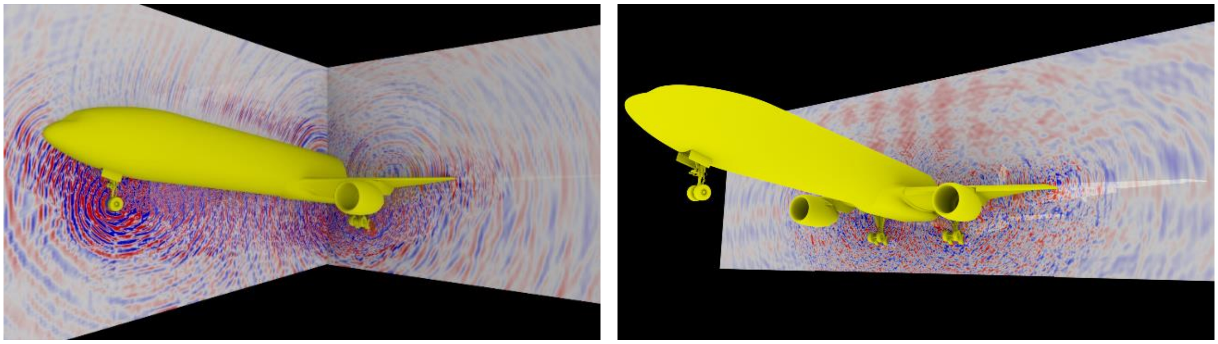

a) Config1 b) Config2

Fig. 13 Instantaneous fluctuating pressure field for full-scale B777-300ER with landing gear deployed.

B. Aerodynamic Results

Convergence time histories of the lift and drag coefficients (C_L and C_D) for Config1 and Config2 are presented in Fig. 14. On the scale used in this figure, xcoarse and coarse simulations produce very similar results, indicating that converged solutions were obtained even at the lowest resolution used. Notice that both C_L and C_D attained their time-averaged levels at approximately 1.5 s. For acoustic analysis, the flow solutions obtained after 1.5 s were collected for the remaining run time, providing 1.0 s of recorded signals. To better highlight the fluctuating lift and drag levels, C_L and C_D are presented on a stretched scale in Fig. 15. As anticipated, the lift and drag forces for Config2 contain lower frequencies and higher amplitude unsteadiness than those computed for Config1. This behavior results from deployment of the high-lift system. In particular, the low-frequency, high-amplitude fluctuations in C_L can be traced to the presence of a large separation zone on the inboard flap segment that was observed first in the 26%-scale STAR model computations of Ref. [12]. The oscillations in extent and strength (breathing) of this separation zone occur on a low-frequency cycle, thus posing a significant computational challenge to the duration of the time records necessary for acoustic analysis.

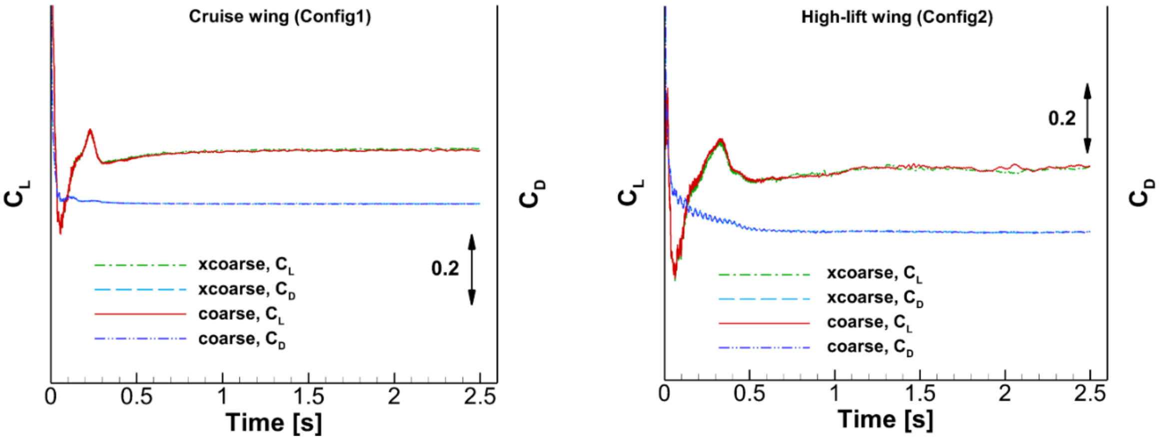

a) Config1 **b) Config2**

Fig. 14 Convergence history of lift and drag coefficients.

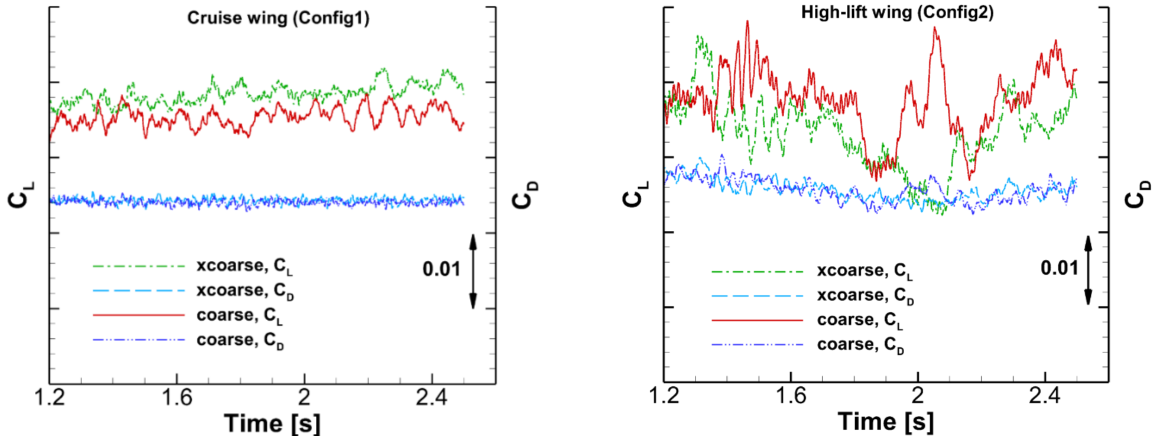

a) Config1 **b) Config2**

Fig. 15 Convergence history of lift and drag coefficients on an expanded scale.

We now examine the time-averaged pressure coefficient (C_P) distribution on the aircraft wing. The lack of measured full-scale surface pressures precluded any direct comparison with experimental data. Thus, we used the predicted surface pressures for the 26% scale B777-200 (STAR) model presented in Ref. [13][7] that were fully validated as an indirect way to demonstrate the accuracy of the present full-scale data. Figure 16 displays the spanwise location of the rows of pressure ports on the STAR model wing. Fortunately, the B777-200 and the present B777-300ER aircraft share the same wing planform up to somewhere between pressure rows 11 and 12. Therefore, data for rows 1 through 11 can be used for comparison purposes. Note, however, that the B777-300ER MLG is slightly different than the STAR model B777-200 gear. Also, the STAR model computations of Ref. [12] were conducted at an angle of attack (AoA) of 7°, whereas the results for Config2 were calculated for AoA = 4°. At low to moderate AoA, in the linear range of the lift curve, flap loading depends solely on the element's deflection relative to the main wing. Thus, we anticipate comparisons of STAR model and full-scale pressures to be relevant for the aft portion of the wing and flaps despite the difference in AoA.

---

[7] The STAR simulations of Refs. [12, 13] were executed at the tested Re = 8.2×10^6 based on model mean aerodynamic chord.

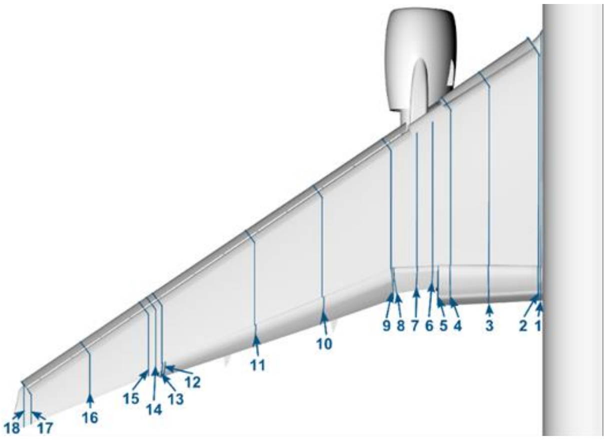

Fig. 16 STAR model wing in landing configuration with pressure port rows used during wind tunnel test. For visualization purposes, some rows were shifted slightly. From Ref. [12].

Time-averaged pressure coefficients for Config2 at four selected rows spanning the entire wing are shown in Fig. 17. The pressures clearly demonstrate the converged nature of the local aerodynamic trends, even at xcoarse resolution, in agreement with the convergence behavior displayed for the integrated forces (Fig. 15).

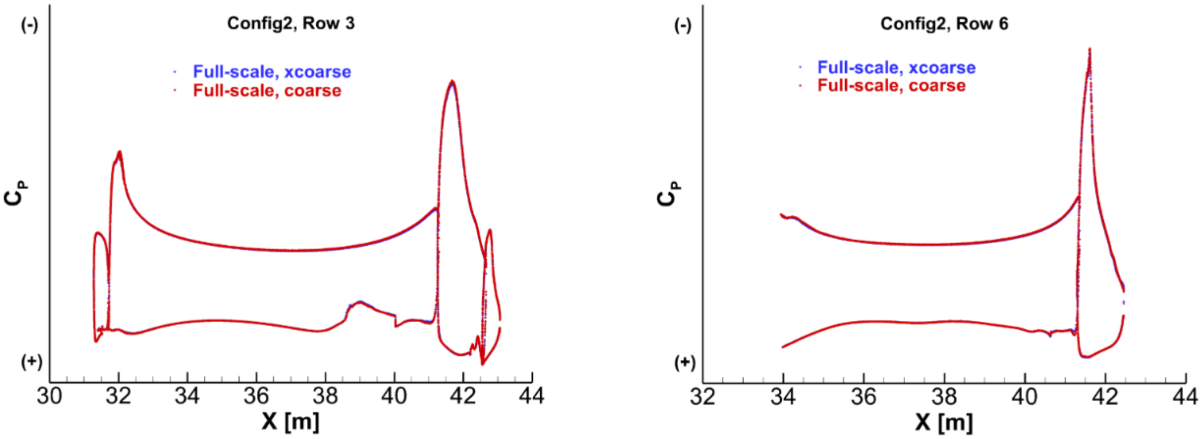

a) Row 3

b) Row 6

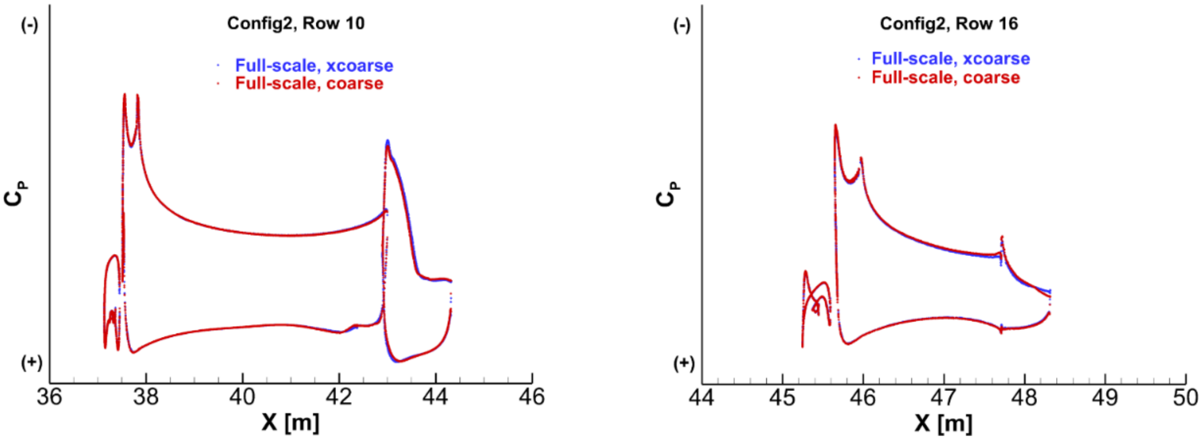

c) Row 10

d) Row 16

Fig. 17 Surface pressure distributions for Config2 wing.

Full-scale pressure distributions at four spanwise locations plotted against computed STAR model data from Ref. [12] are shown in Fig. 18. For comparison purposes, the STAR model pressure coordinates have been converted to their equivalent full-scale coordinates. As indicated previously, the model-scale pressures are in excellent agreement with wind tunnel measurements of the STAR model (see Ref. [13]) and therefore should be viewed as equivalent to the experimental data. As expected, the leading-edge slat and most of the wing experience reduced loading due to the lower AoA in the present data. At row 3 (Fig. 18a), where significant gear-flap flow interaction exists, noticeable differences in the pressure levels for the aft portion of the wing and flaps, caused by differences in AoA, impingement of MLG wakes on the flaps, and Reynolds number effects, are observed. For regions not affected by the MLG wakes (Figs. 18b, 18c, and 18d), there is remarkable agreement in aft wing and flap loading between STAR model and present full-scale simulation results. The subtle increases in pressure magnitude near the wing trailing edge and the suction side of the flaperon (row 6, Fig. 18b) and flap (rows 10 and 11, Figs. 18c and d) are caused mainly by the higher Re of the full-scale simulation. The Cp results displayed in Fig. 18 clearly corroborate our earlier assertion that a Re that is at least 30%-40% of flight Re is sufficient to capture most of the aeroacoustic trends of interest, as demonstrated for a different class of aircraft in Ref. [18].

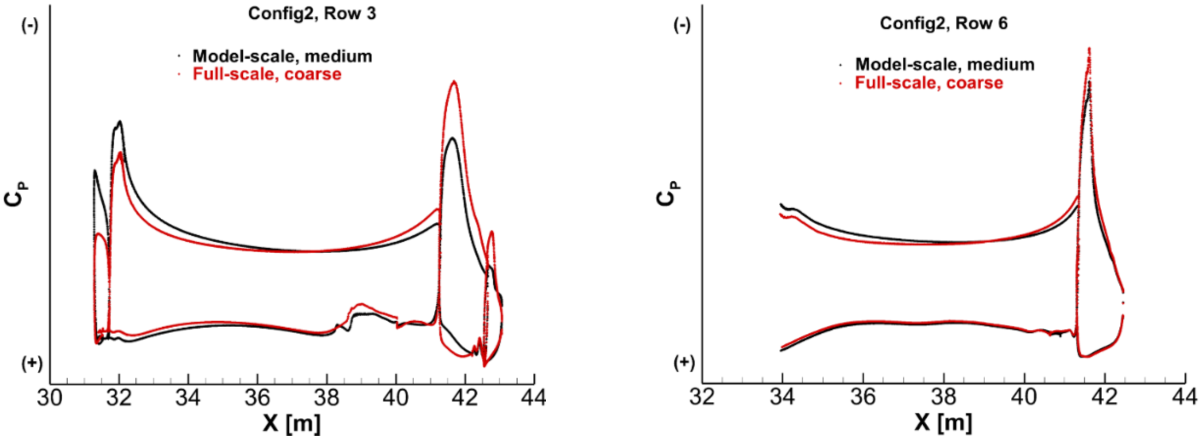

a) Row 3 **b) Row 6**

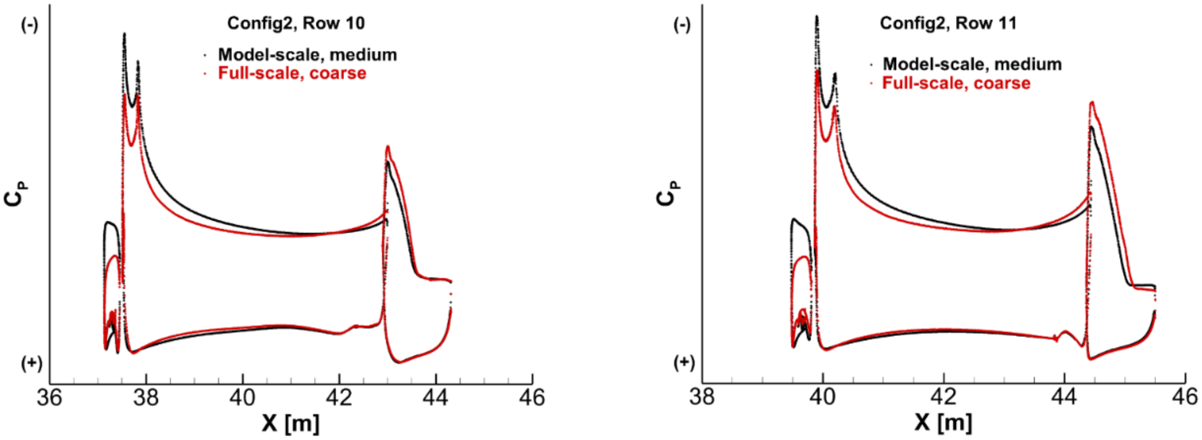

c) Row 10 **d) Row 11**

Fig. 18 Comparison of full-scale surface pressure distribution (Config2) with simulated pressures for 26% scale STAR model from Refs. [12, 13]. Chordwise coordinates for model-scale pressures have been converted to their corresponding full-scale values.

C. Acoustic Results

In this section, we identify the primary airframe noise sources and their relative strength through beamform maps calculated on the Wing and Gear planes described in Section IIIc, followed by a detailed discussion of integrated far-field spectra.

1. Source Localization (Beamform) Maps

All CLEAN beamform maps were generated in narrowband (with 50 Hz resolution). Those results were used to generate the maps in 1/12th-octave bands presented in this section. Only sample maps at select frequencies are shown. These carefully chosen maps are sufficient to highlight the key trends that affect the aircraft far-field noise signature.

Sample CLEAN maps for Config1 at frequencies (f) of 355 Hz, 450 Hz, 1,060 Hz, and 2,000 Hz are presented in Fig. 19. To assess spatial resolution effects, maps obtained from xcoarse and coarse simulations are shown side by side. Unless specified otherwise, a 10 dB cutoff from the peak level was used for all maps included in this paper. For ease in visualization, the absolute level corresponding to 0 dB was the same for each pair of maps. Note from Fig. 19 that, with high-lift devices retracted (cruise wing), the NLG and MLG emerge as the two primary and dominant airframe sources, as expected. The NLG produces a major tone around 450 Hz (Fig. 19d) that is several dB louder than other sources. For frequencies up to 1,100 Hz, the xcoarse and coarse beamform source maps are similar in both distribution and strength. Above 1,100 Hz, increasing the spatial resolution significantly improves the high-frequency content of the noise emitted by the NLG and MLG. Sample beamform maps from coarse simulations showing the effect of installing toboggan fairings on the Config1 MLG are shown in Fig. 20 for a frequency of 1,800 Hz. Note from the figure that substantial changes in the strength of the MLG sources do not result from application of the toboggan. Maps generated at other frequencies (not shown) indicated a similar trend.

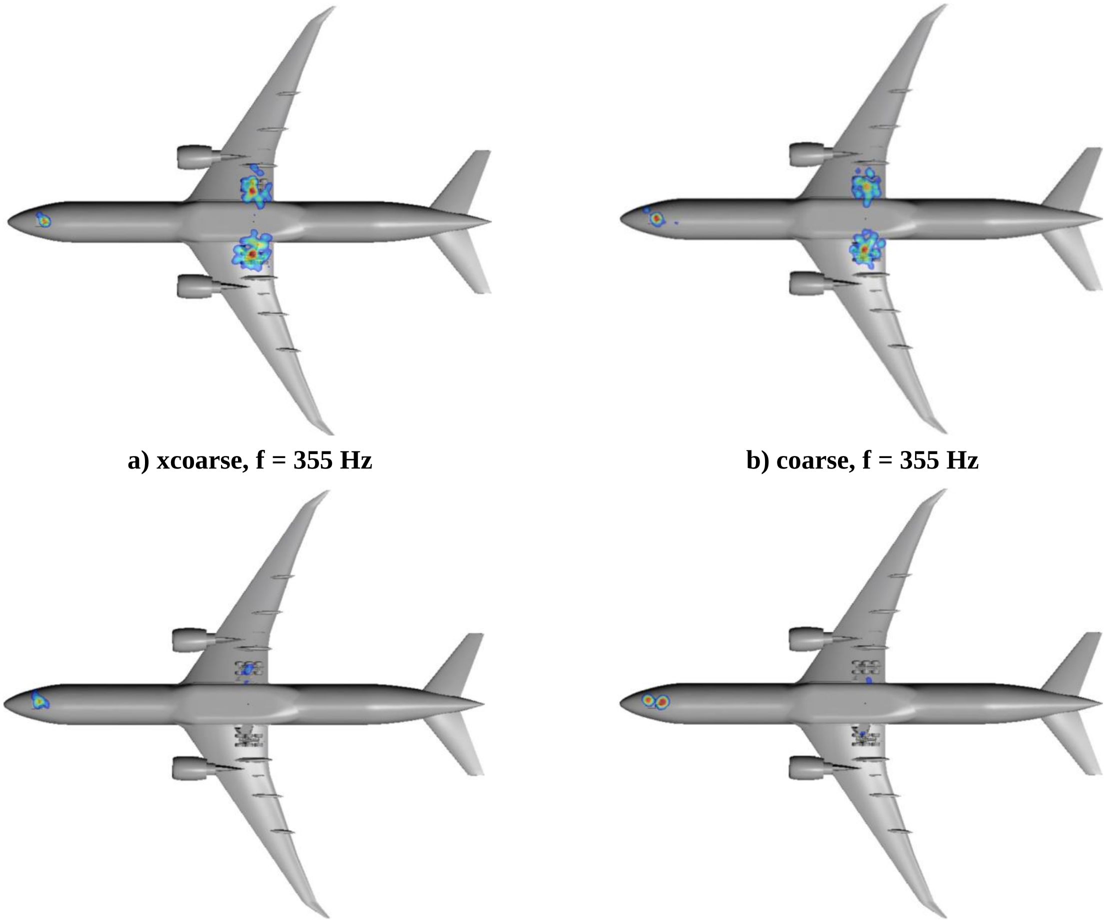

a) xcoarse, f = 355 Hz

b) coarse, f = 355 Hz

c) xcoarse, f = 450 Hz

d) coarse, f = 450 Hz

Fig. 19 Effect of spatial resolution on CLEAN maps at various frequencies for Config1.

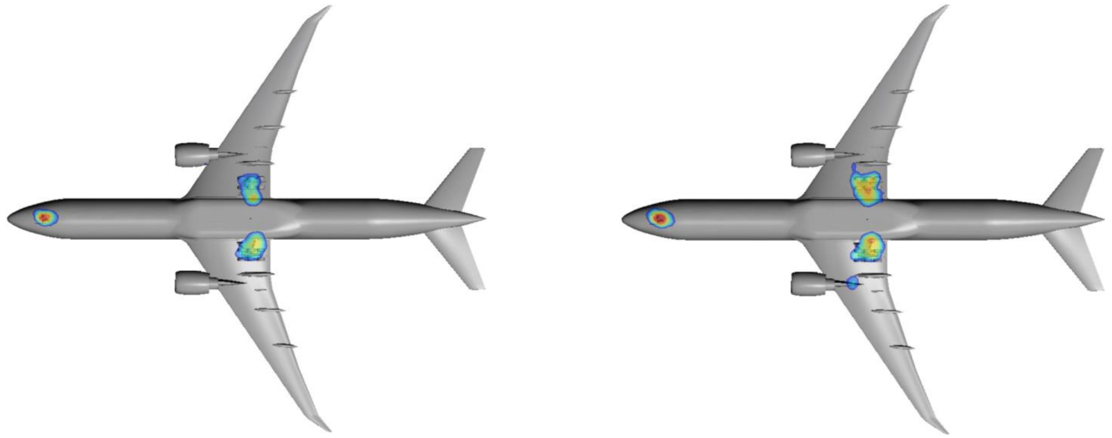

e) xcoarse, f = 1,060 Hz

f) coarse, f = 1,060 Hz

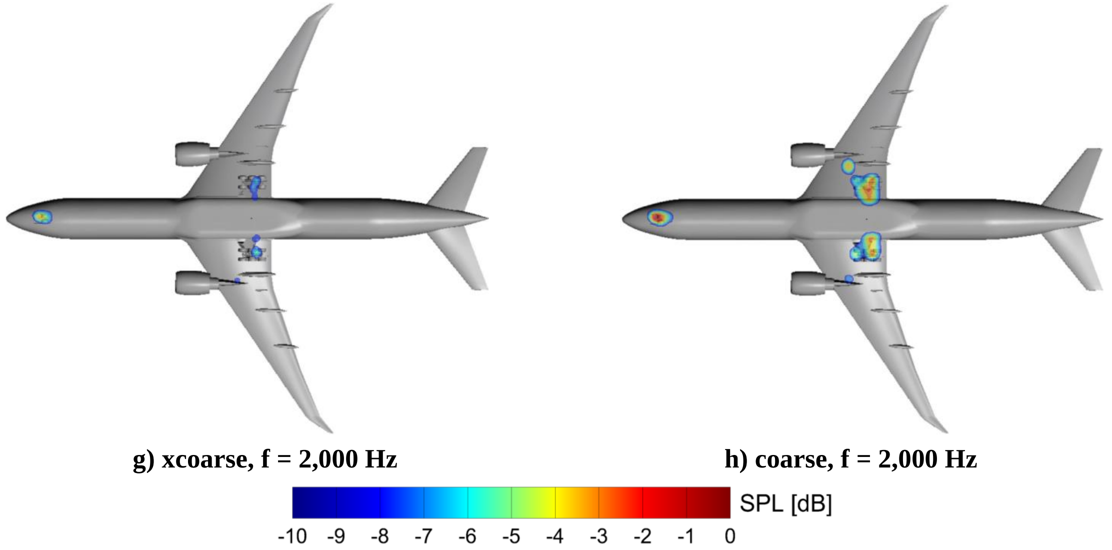

g) xcoarse, f = 2,000 Hz

h) coarse, f = 2,000 Hz

Fig. 19 Concluded.

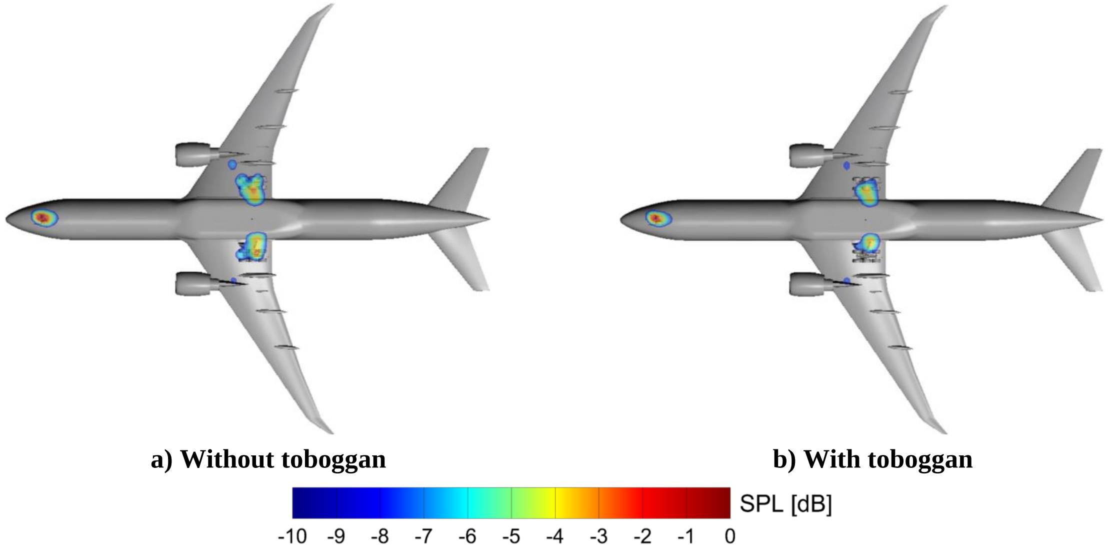

a) Without toboggan

b) With toboggan

Fig. 20 Effect of toboggan fairings on MLG noise for Config1, f = 1,800 Hz. CLEAN maps obtained from coarse simulations.

Sample CLEAN maps for Config2 at frequencies of 500 Hz, 1,180 Hz, 2,240 Hz, and 3,550 Hz are shown in Fig. 21. As in Fig. 19, maps from xcoarse and coarse simulations are displayed as pairs for each frequency of interest. Although not shown, the lower aircraft speed of Config2 shifted the frequency of the NLG tone observed in Fig. 19d from the 450 Hz bin to 400 Hz, suggesting that it is a flow-induced tone (e.g., bluff body vortex shedding) and not caused by cavity resonance. The map at 500 Hz (Fig. 21a) contains noise sources in addition to the NLG and MLG that are generated by deflection of the slats and flaps. Most notable among these sources are the slat brackets in the outboard segment of the wing, as well as sources residing at the inboard and outboard flap tips. When compared to Config1, the Config2 maps clearly show noticeable reductions in the strength of MLG sources relative to those from the NLG. As will be shown later, this behavior resulted from the deployment of flaps at their highest deflection angles, which significantly altered the local flow around the MLG. Also note from Fig. 21 that, as observed for Config1, increasing spatial resolution yields significant improvement in the definition of MLG sources at frequencies above 1,100 Hz. Moreover, at the coarse resolution level, the simulation captures prominent tonal features associated with the MLG component. These high-amplitude oscillations will be discussed in section IV.C.2.b

A sample CLEAN map from a coarse simulation with the toboggan fairing installed is compared with untreated Config2 data in Fig. 22 for a frequency of 1,180 Hz. Since the MLG produces less noise when the flaps are deflected, only negligible changes in noise levels result from application of the toboggan fairing. This insignificant change in source strength was observed in maps spread over a wide frequency range.

The implications of permeable data surface choice for Config2 acoustic results are demonstrated in Fig. 23 via sample CLEAN maps generated from xcoarse simulation data for frequencies of 1,120 Hz and 2,650 Hz. The maps on Figs. 23a and 23c were computed from data collected on the nominal permeable surface used for both configurations (red line contours in Fig. 5), while those on Figs. 23b and 23d were generated using the expanded permeable surface for Config2 (blue line contours in Fig. 5). Observe that, for frequencies below 2,500 Hz (Figs. 23a and 23b), both permeable data surfaces produce maps that are nearly indistinguishable. However, at frequencies above 2,500 Hz (Figs. 23c and 23d), maps obtained from the nominal permeable surface contain spurious sources that are caused by the passage of large-scale hydrodynamic flow structures through the bottom boundary of this data surface. The map in Fig. 23c clearly shows the appearance of these numerical sources, which are caused by inboard flap tip vortices exiting the surface due to the strong downwash associated with deployment of the high-lift system. As shown in Fig. 23d, these spurious sources disappear for the permeable data surface that encompasses a larger volume underneath the aircraft. As will be demonstrated in the following section, use of the tailored integration regions presented in Fig. 10 eliminates most of the contributions from the spurious sources to the far-field spectra.

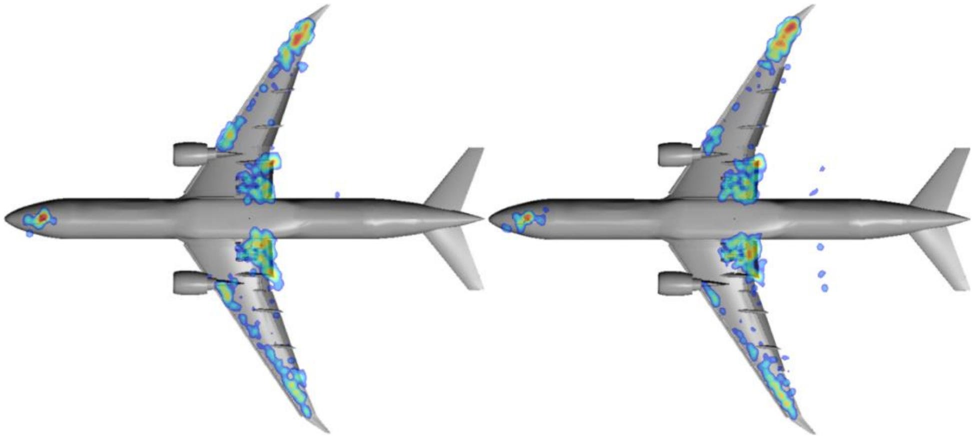

a) xcoarse, f = 500 Hz **b) coarse, f = 500 Hz**

Fig. 21 Effect of spatial resolution on CLEAN maps at various frequencies for Config2.

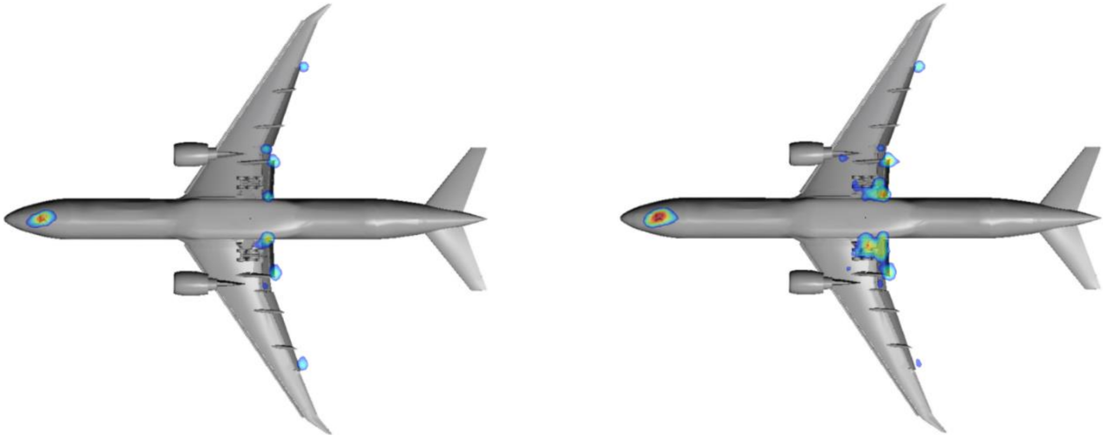

c) xcoarse, f = 1,180 Hz

d) coarse, f = 1,180 Hz

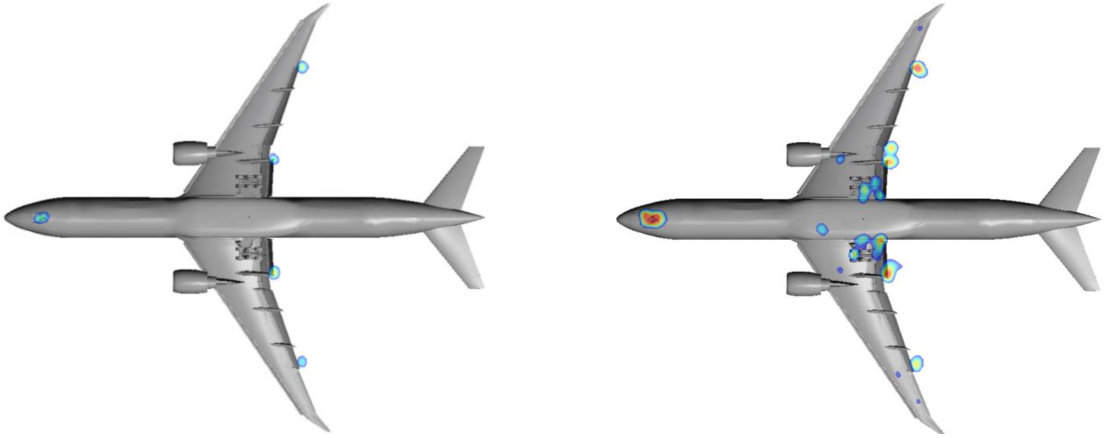

e) xcoarse, f = 2,240 Hz

f) coarse, f = 2,240 Hz

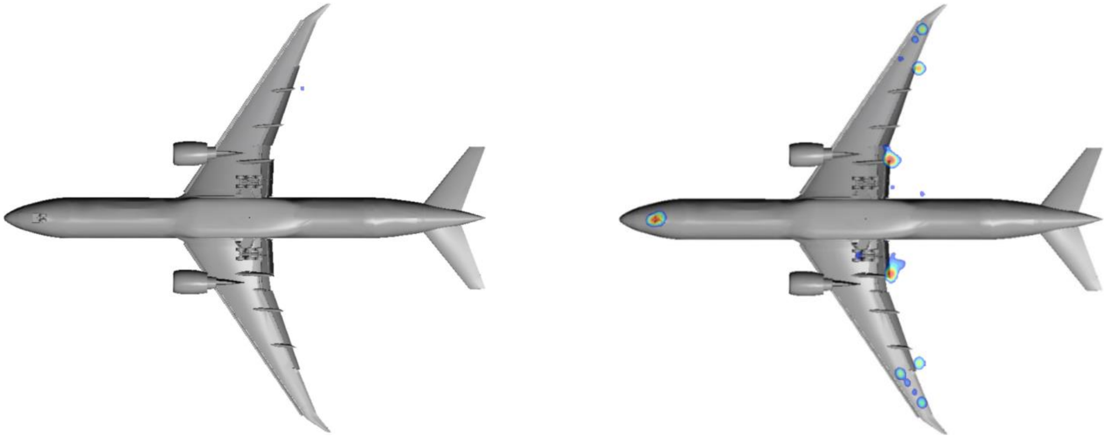

g) xcoarse, f = 3,550 Hz

h) coarse, f = 3,550 Hz

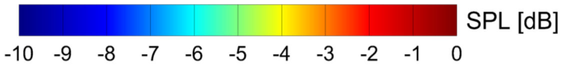

Fig. 21 Concluded.

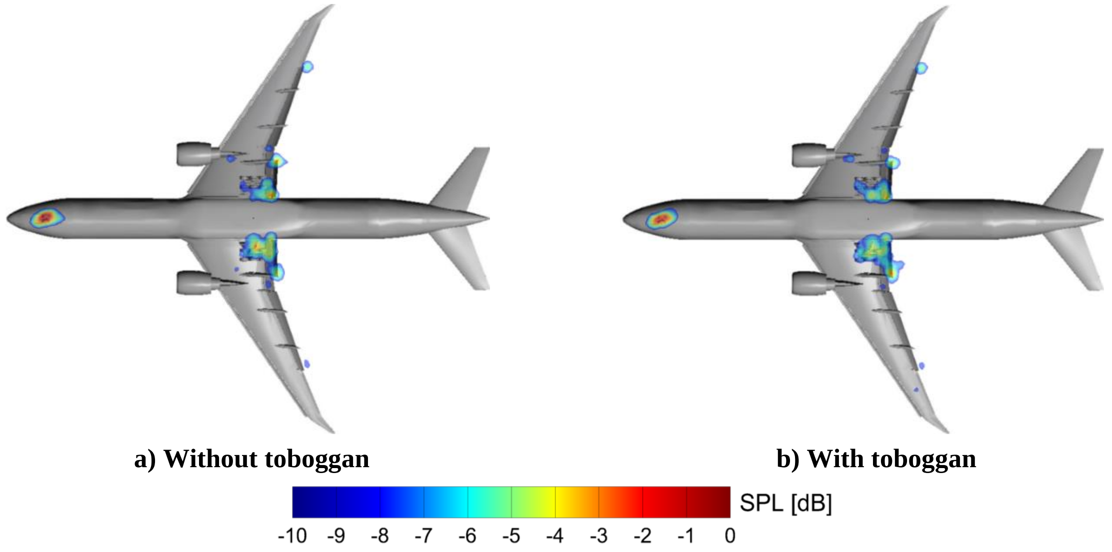

a) Without toboggan **b) With toboggan**

Fig. 22 Effect of toboggan fairings on MLG noise for Config2, f = 1,180 Hz. CLEAN maps obtained from coarse simulations.

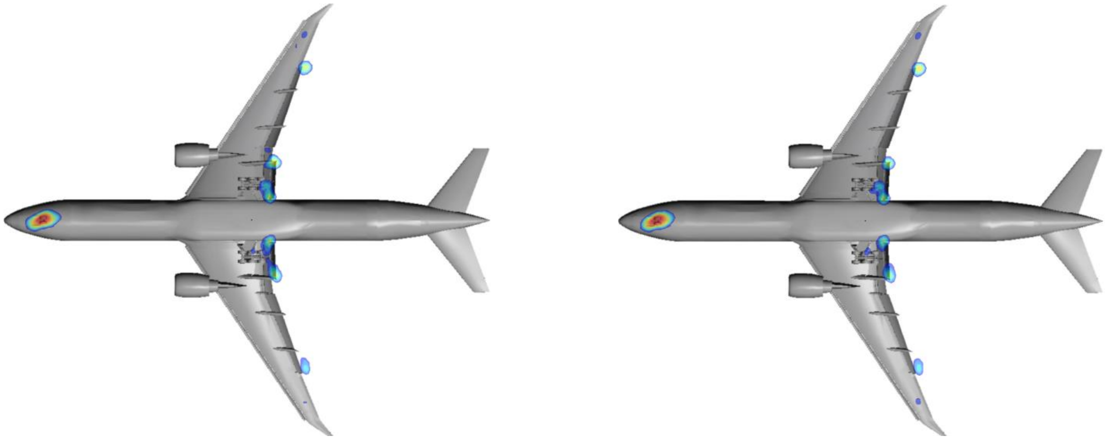

a) Nominal, f = 1,120 Hz **b) Expanded, f = 1,120 Hz**

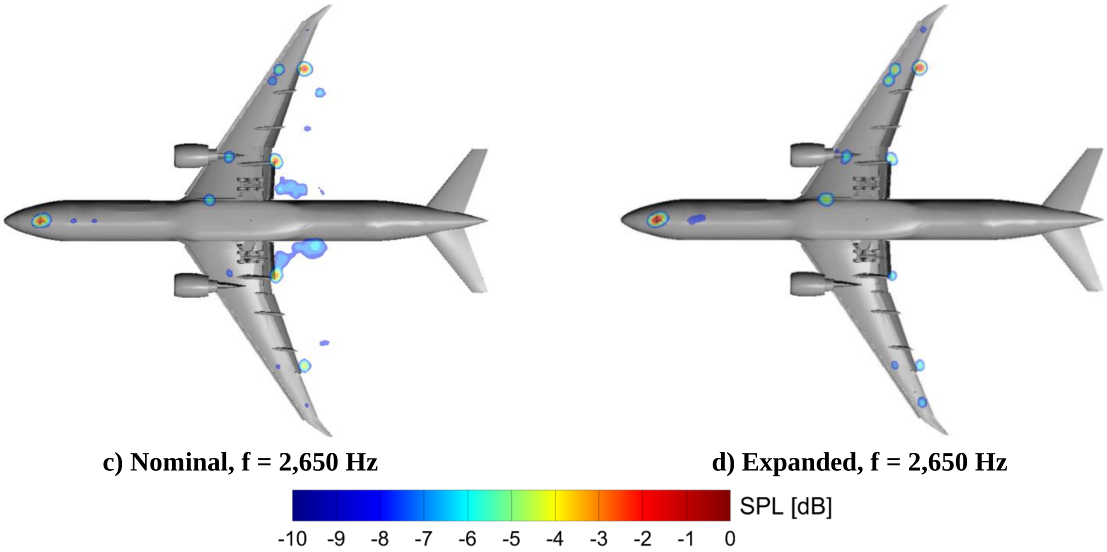

c) Nominal, f = 2,650 Hz **d) Expanded, f = 2,650 Hz**

Fig. 23 Effect of permeable surface extent for Config2. CLEAN maps obtained from xcoarse simulations.

2. Integrated Far-Field Noise Spectra

Far-field spectra obtained from integration of narrowband CLEAN maps for various regions defined in Fig. 10 are presented in this section. The main focus of the analysis is the quantification of noise emanating from the aircraft undercarriage. Unless specified, the spectra were computed from maps obtained for the “Gear” plane with an integration cutoff of 10 dB from the peak in the region being integrated.

a. <u>Cruise-wing with Landing Gear Deployed (Config1)</u>

The far-field noise signature for Config1 is shown in Fig. 24a, which presents spectra obtained from integration of the “Whole Grid” (see Fig. 10a) and the “Sum” of the smaller regions containing the NLG, MLG, and aircraft wings (regions 1-9 in Fig. 10a) for the two simulated resolutions. Notice that the spectrum based on the entire grid was obtained with cutoff ranges of 10 dB and 15 dB, the latter done to determine the contribution of weaker sources that may have been excluded with the narrower cutoff. Observe that a cutoff of 10 dB is sufficient to capture most of the noise generated by this aircraft configuration. As expected, a more accurate picture of the high-frequency component of the noise emerges with increased spatial resolution. In Fig. 24b, coarse resolution spectra based on the “Whole” and “Sum” integration regions are compared with levels obtained from the landing gear only (regions 1, 5, and 6 in Fig. 10a), represented by the “all gears” spectrum. The plots clearly indicate that, for Config1, the landing gear are responsible for the entire acoustic field measured on the ground. The small differences in the levels at frequencies below 300 Hz can be attributed to array resolution and/or side lobes from the gear sources that are included in the integrated levels when the larger regions are considered.

The far-field noise signature of the NLG only (region 1 in Fig. 10a) is displayed in Fig. 25a. The tone at 450 Hz noted in the beamform maps (Fig. 19b) is clearly visible in the figure. In Fig. 25b, spectra from the present computations are compared with isolated NLG results from Ref. [14] that were obtained at comparable and higher spatial resolutions. The comparison is possible because the same flight conditions were used for both computational studies. Recall from section III.A that the spatial resolution near the NLG surface had to be relaxed slightly in order to arrive at a reasonable grid size for the entire aircraft. As observed in Fig. 25b, this degradation in spatial resolution caused the present xcoarse spectrum to under-predict the noise levels reported in Ref. [14] for frequencies above 1,500 Hz. However, the present coarse resolution seemed sufficient to produce a spectrum that closely tracks the coarse resolution spectrum from Ref. [14].

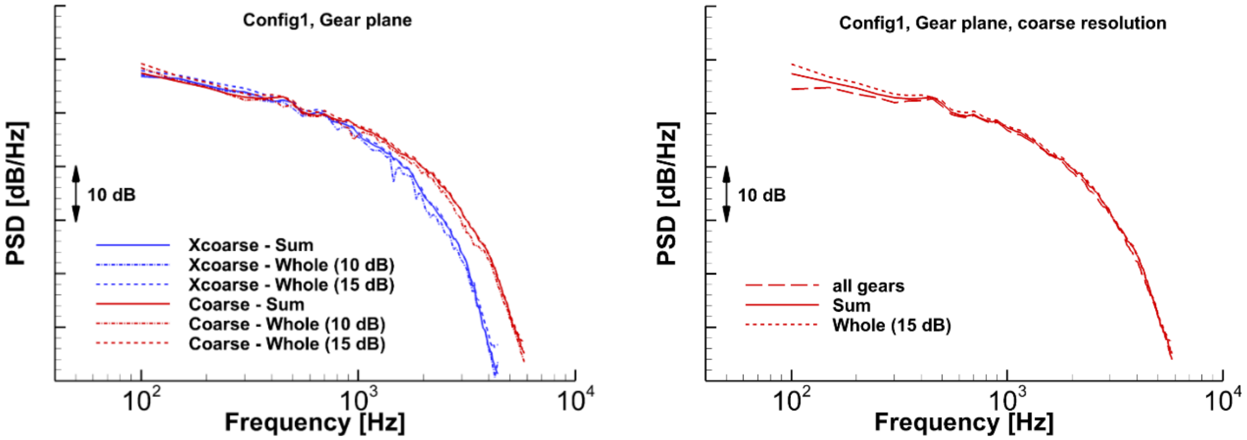

a) Cutoff effect **b) Landing gear effect**

Fig. 24 Far-field noise spectrum from integrated levels for Config1. Spectra in plots on the right obtained from coarse simulation.

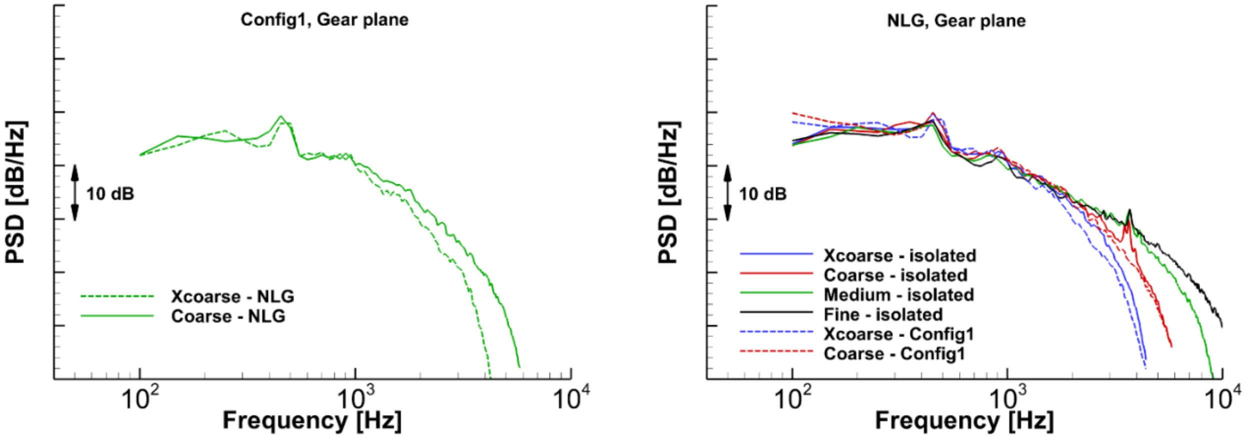

a) Present study **b) Comparison with isolated gear from Ref. [14]**

Fig. 25 Effect of spatial resolution on integrated far-field spectra for NLG component of Config1.

The far-field noise footprint of the port and starboard MLGs (regions 5 and 6 in Fig. 10a) are shown in Fig. 26 for configurations without (baseline) and with toboggan fairing. Notice that increasing spatial resolution results in better toboggan performance. This trend stems from improved definition of the higher-frequency noise content that is now shielded more effectively by the toboggan. Also observe from Fig. 26 that, upon closer scrutiny, the spectra from the port and starboard MLGs reveal slight differences in noise levels. These differences are attributed to the lateral offset of the aircraft position relative to the array center during the flyover (see Fig. 6a). To determine the impact of this lateral offset on far-field noise spectra, the beamform maps and integrated spectra were recomputed based on synthetic pressure records generated for a ground array centered between the two MLG. The landing gear spectra computed from the centered array are compared to those obtained with the synthetic array in its flight-test position in Fig. 27. Note that array displacement does not seem to affect the broadband component of NLG noise (Fig. 27a). However, the amplitude of the NLG-produced tone centered at approximately 450 Hz increased significantly, suggesting a strong dependence on the lateral and/or flyover directivity angles. Minor differences between port and starboard MLG synthetic spectra that were obtained with the flight test array (Fig. 27b) practically vanished for frequencies above 500 Hz when the centered array was used (Fig. 27c). This trend confirmed our earlier assertion that the subtle differences observed in the noise produced by the port and starboard sides of the aircraft were caused by the lateral offset of the ground array. The relative contribution of each gear to the far-field noise is presented in Fig. 28 with spectral levels adjusted to a common height of 120 m. At frequencies below 1,400 Hz, levels generated by the NLG are 4 to 5 dB lower than those produced by each MLG. Above 1,400 Hz, NLG levels are more or less equivalent to those of each MLG. The spectra indicate that the NLG becomes the dominant source at frequencies above 3,500 Hz. Unfortunately, due to insufficient spatial resolution, we cannot ascertain whether the NLG is indeed louder than either MLG at frequencies higher than about 3,000 Hz.

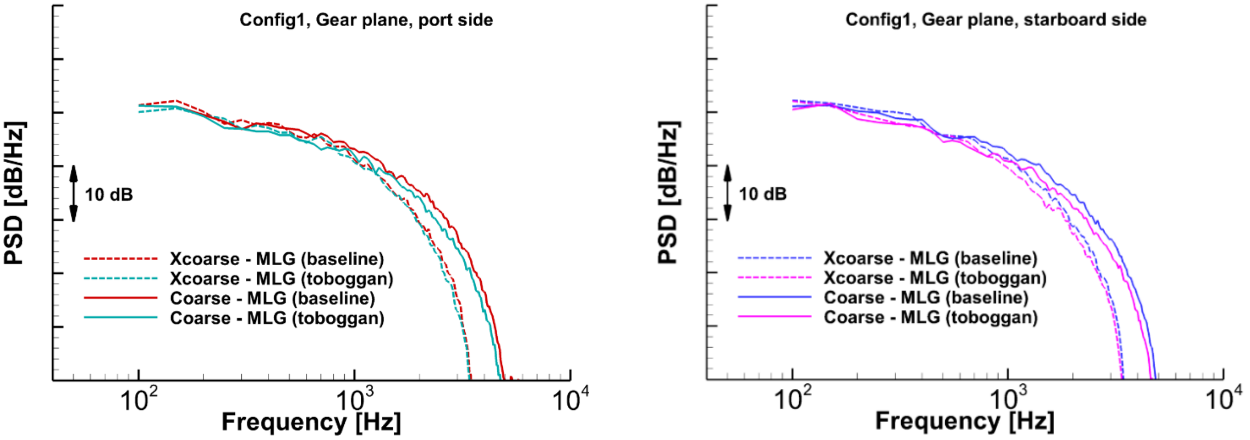

a) Port MLG **b) Starboard MLG**

Fig. 26 Effect of toboggan fairing on integrated far-field spectra for MLG component of Config1.

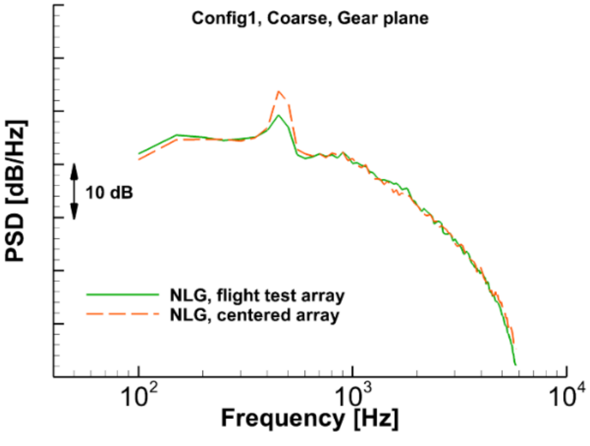

a) NLG

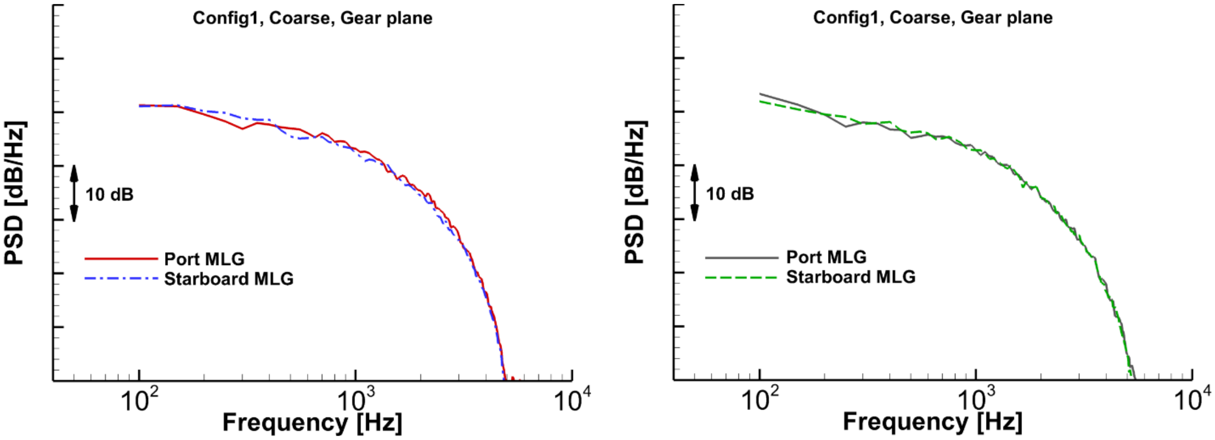

b) MLG, flight test array

c) MLG, centered array

Fig. 27 Effect of aircraft lateral position relative to microphone array center on integrated far-field noise spectra of Config1. Results from coarse simulation.

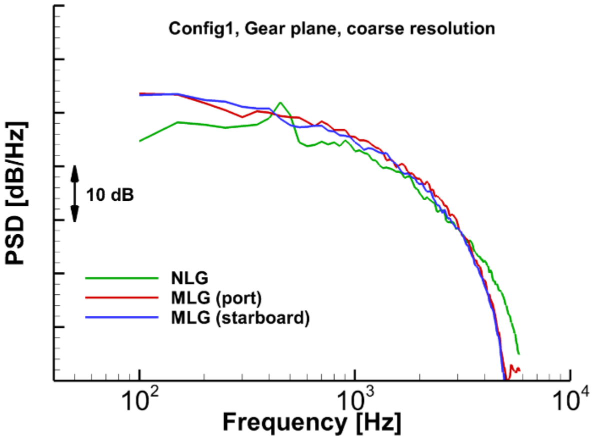

Fig. 28 Comparison of noise levels generated by NLG and MLG components of Config1. Results from coarse simulation with spectral amplitude adjusted to a height of 120 m.

b. High-Lift Wing with Landing Gear Deployed (Config2)

Total integrated noise levels produced by Config2 are presented in Fig. 29a. Unlike Config1 at frequencies above 2,500 Hz (Fig. 24a), levels obtained from integrating the entire (Whole) grid are 2–3 dB higher than those from the “Sum” of all sub-regions defined in Fig. 10a. These differences are mainly due to the presence of spurious (numerical) sources downstream of the wing trailing edge, as shown in Fig. 23c. The far-field noise spectra obtained from nominal permeable surface data are compared with those from expanded permeable surface data in Fig. 29b. Notice that extending the permeable surface below the aircraft eliminates the spurious sources that were produced by the passage of strong hydrodynamic flow fluctuations through the bottom segment of the nominal surface. More importantly, observe that the “Sum” of contributions from the integration sub-regions defined in Fig. 10a is nearly identical between the two permeable data surfaces. The trends depicted in Fig. 29b confirm our assertion that the devised integration regions produce an accurate representation of the Config2 aircraft noise levels, even when using data from the nominal permeable surface. The spectra produced by the NLG and the MLG without contributions from the flap side-edges (region 5b and 6b in Fig. 10b) are shown in Figs. 30a and 30b, respectively. Due to lower aircraft speed, differences in aircraft conditions, and deployment of high-lift devices, the convergence behavior of NLG noise with increased resolution is slightly different than that displayed for Config1 (see Fig. 25a); however, at the coarse resolution level, the NLG noise spectrum attains a similar shape for both aircraft configurations. The MLG far-field noise spectra (Fig. 30b) show that the gear on the starboard side produces higher noise levels than the port gear. Again, this difference is entirely caused by the aircraft lateral offset relative to the array center (Fig. 6b). Observe also from Fig. 30b that the MLG spectra computed from coarse resolution array data show numerous prominent tones over a wide frequency range. Closer examination of the MLG spectra revealed that these tones were multiples (higher harmonics) of a fundamental frequency of 314 Hz. To determine the source of these tones, with the array focused on the starboard MLG, the beamform maps at several of the tonal frequencies were carefully examined. A sample map obtained at 1,900 Hz (the 6th harmonic) is shown in Fig. 31a. The maps pointed to a juncture area where several major subcomponents (e.g., drag/side braces and shock strut retract actuator) attach to the main post. These subcomponents feature several small, round openings at their junctures, as shown in Fig. 31b. Animations of the surface pressure fluctuations, similar to the instantaneous frames presented in Fig. 12, revealed that most of these openings were pulsating at fixed frequencies. To illustrate the connection between these openings and the tones in the MLG far-field spectra, the recorded fluctuating surface pressures were band-filtered for the frequency bands of 920–960 Hz and 1,860–1,900 Hz, which represent two of the more prominent tones. For both bands, the highest-amplitude surface pressures occurred in the pinhole of the shock strut retract actuator shown in Fig. 31b. The pinhole is open on both sides and has chamfered edges. A thin bolt spans the diameter of the rear opening, as shown in the insert of Fig. 31b. The pinhole has a constant radius, r, of 19.06 mm and a length (excluding the short chamfers), L, of 506.7 mm. Geometric information was used to determine the first resonant frequency for an unflanged open–open pipe [25], which is given by:

$$f = \frac{c}{2(L + 2l_0)} \qquad (1)$$

Where c is the speed of sound (341.95 m/s for Config2) and l_0 is the end correction given by:

$$l_0 = 0.61r \qquad (2)$$

From Eq. (1), the fundamental frequency of the resonance is 322.6 Hz, which is very close to the 314 Hz deduced from the simulated MLG spectra. This small difference in frequency could be caused by the bolt across the rear opening and other subtle geometrical differences with an ideal open-open pipe. The small flange on the forward-facing end of the pinhole may also impact this value. Corrections for flow through the pinhole would be relatively small and were ignored for this simplified analysis.

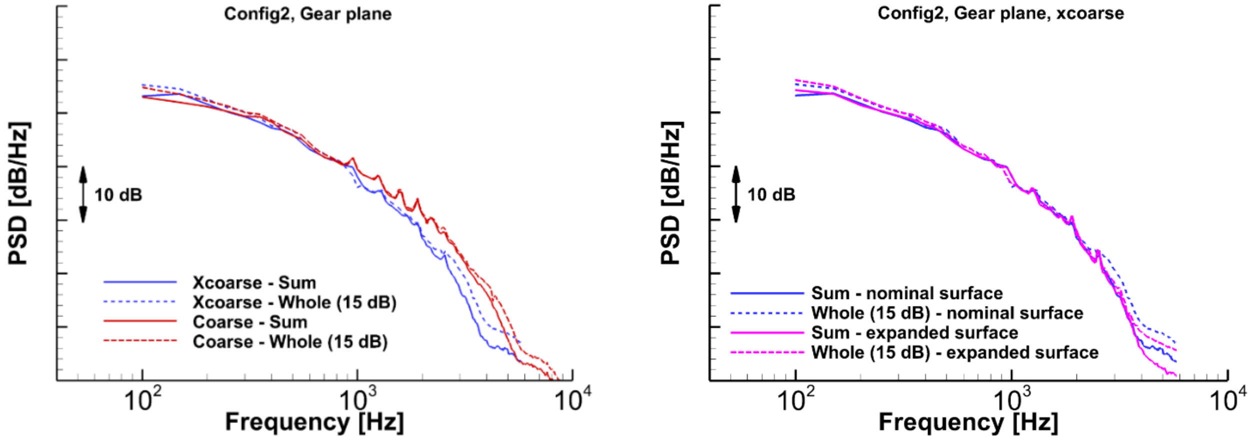

a) Nominal surface b) Nominal vs. expanded surfaces

Fig. 29 Influence of integration region and permeable data surface extent on the far-field noise spectrum of Config2. Spectra in plots on the right obtained from xcoarse simulation.

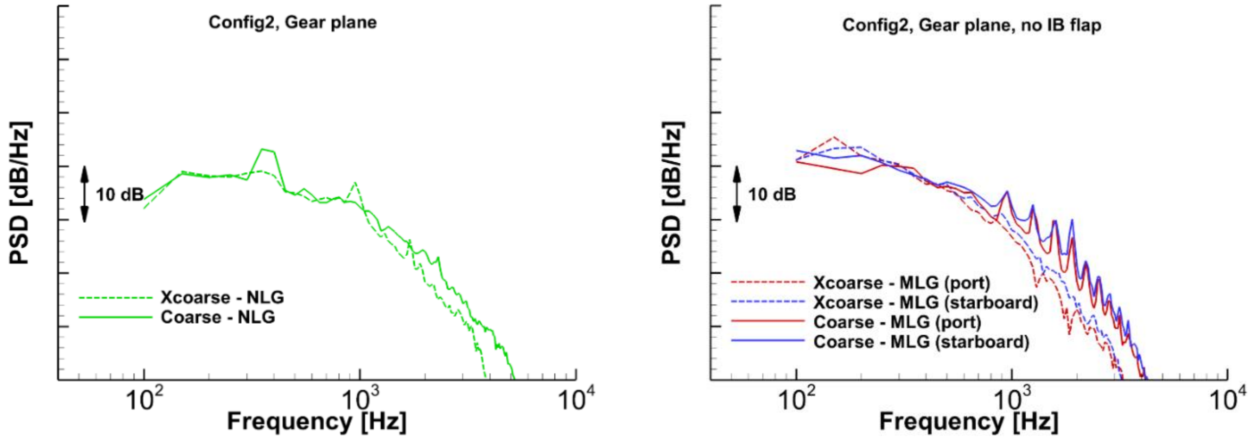

a) NLG b) MLG

Fig. 30 Integrated far-field spectra for NLG and MLG components of Config2.

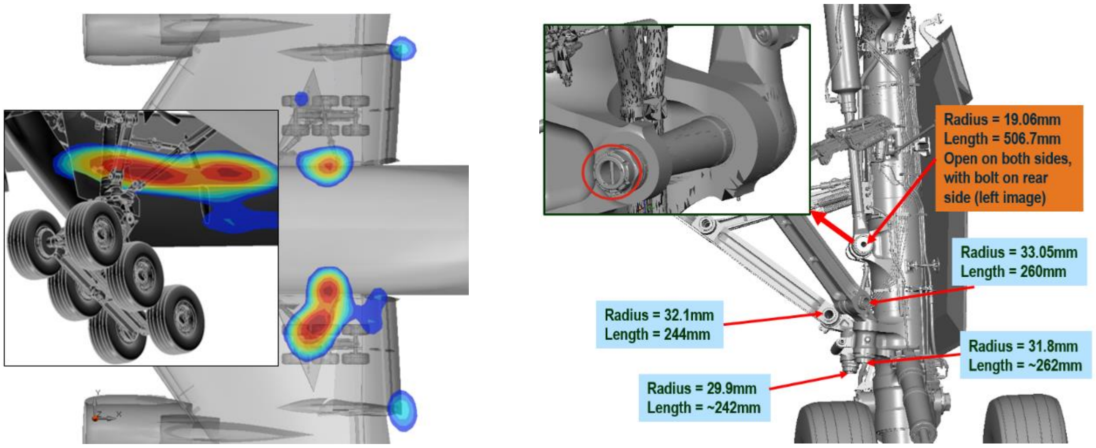

a) Beamform map at f = 1,900 Hz b) Sources of resonance

Fig. 31 Close-up view of Config2 MLG.

A comparison of integrated noise levels obtained from the “Gear” and “Wing” planes (Fig. 7) is shown in Fig. 32. Note that both planes produced very similar spectra, indicating a lack of meaningful array resolution in the direction normal to the planes. Inboard flap tip source contribution to the noise obtained from integration of the port side MLG region (Fig. 10b) is presented in Fig. 33a. Although the inboard flap tip sources are substantially weaker than MLG sources, they provide a noticeable contribution to the total noise emanating from the MLG region. The contributions of individual gears to the total noise generated by the Config2 aircraft are depicted in Fig. 33b with spectral levels adjusted to a common height of 120 m. Two important points are worth highlighting in this figure. First, across the entire frequency range, the combined contribution of all three gears is 3–4 dB lower than the “Sum” of all sources, indicating the importance of the noise generated by the high-lift components. Second, the noise produced by the NLG is equivalent to, and at higher frequencies even stronger than, the noise generated by either MLG. This trend contrasts with that observed for Config1 (Fig. 28). Since the NLG sources remain relatively unchanged between the two aircraft configurations, then the MLG sources have become weaker. This reduction in source intensity was caused, most likely, by the effect that slat and flap deflection had on the local flow field impinging on the main gears. The integrated spectra for the port and starboard MLGs without and with toboggan fairings are presented in Fig. 34. In contrast to the results observed for Config1 (Fig. 26), application of the toboggan did not produce a measurable reduction in MLG noise. This behavior is in general agreement with the QTD2 flight test measurements of Ref. [4]. It is unfortunate that medium-resolution simulation results are not available to determine whether the aeroacoustic performance of the toboggan fairing improves when the noise sources at frequencies above 2,500 Hz are characterized better.

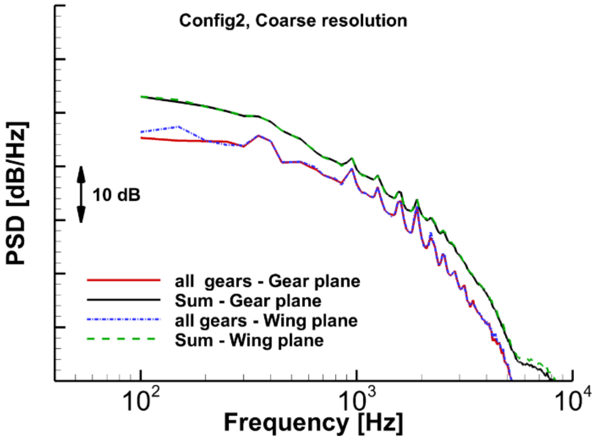

Fig. 32 Influence of integration plane position on far-field noise spectrum of Config2.

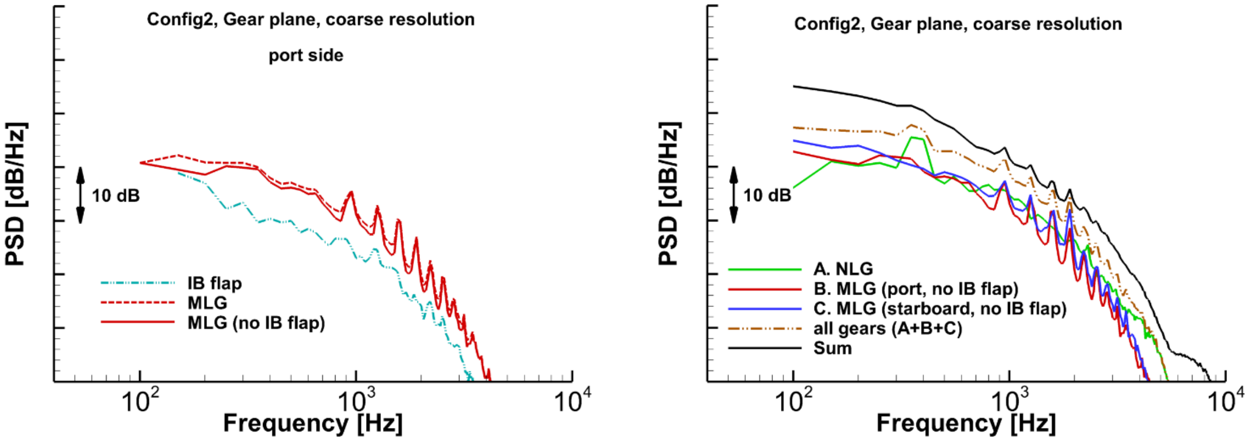

a) Effect of flap side-edge on port MLG noise

b) Contribution of undercarriage to total noise (spectral amplitude adjusted to 120 m.)

Fig. 33 Integrated far-field spectra for Config2. Results from coarse resolution simulation.

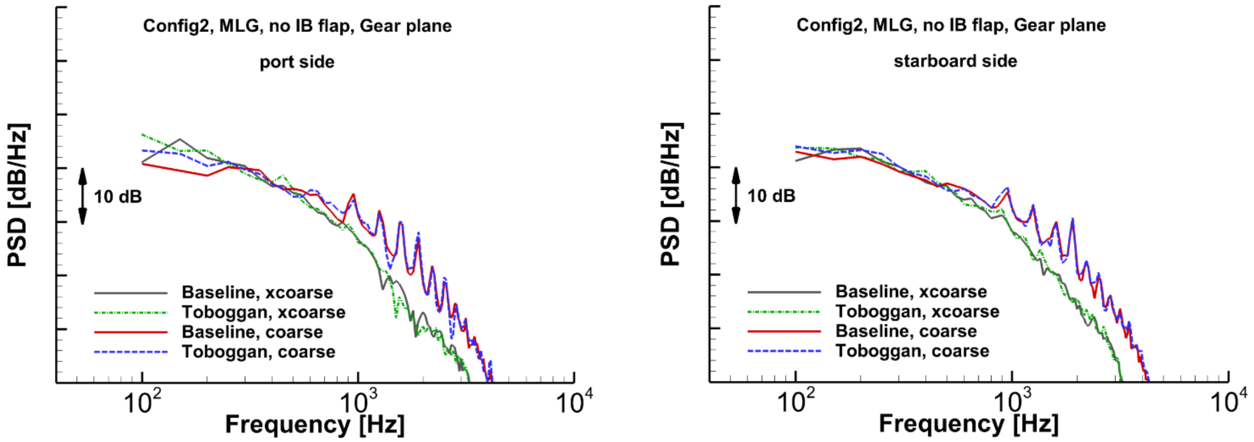

a) Port MLG **b) Starboard MLG**

Fig. 34 Effect of toboggan on integrated far-field spectra for the MLG component of Config2.

An in-depth analysis of the synthetic noise sources associated with the high-lift devices was not attempted because, ultimately, the predicted trends cannot be validated against experimental data: recall that the simulated slat and flap brackets were scaled up from the 26% STAR model and, as such, do not correspond to the actual components flown during the flight tests described in Ref. [4]. As noted in section I, validation of the predicted noise signatures produced by the NLG and MLG with measured microphone array data [4] is provided in a companion paper [16]. The only results presented here are far-field noise spectra obtained from integration of the "Outboard Wing" regions (sections 2 and 9 in Fig. 10a) to highlight a computational challenge faced during simulation of highly complex aircraft configurations. These spectra are shown in Fig. 35a. As expected, increasing spatial resolution yields significant improvement in the predicted noise levels at frequencies above 1,500 Hz. Notice also the presence of prominent tones in the xcoarse spectrum on the starboard wing (a similar behavior was observed for the port wing on a separate xcoarse simulation of Config2). The sources of these tones were traced to the presence of small openings in the 5th and 6th slat brackets from the wing tip (Fig. 35b). The slat bracket resonance, which has a fundamental frequency of 630 Hz and seems to be reflected by the flap, was caused by under-resolution of these small openings. As can be seen in Fig. 35a, the tones and their reflections disappear at a higher (coarse) spatial resolution. The apparent resonance from the slat brackets exemplifies the need to conduct simulations at several spatial resolutions in order to characterize properly the aeroacoustic behavior of complex geometries that contain numerous cavities, openings, and/or gaps of various sizes and shapes.

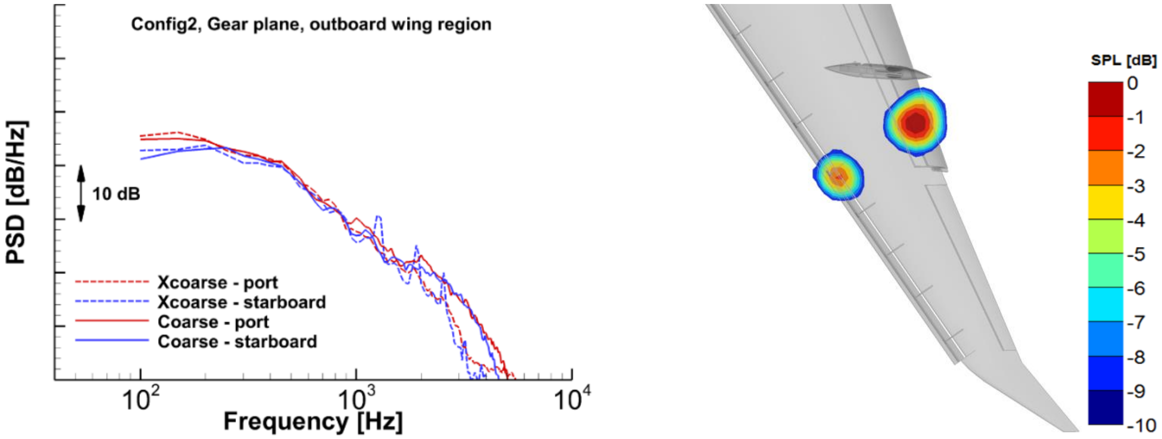

a) Far-field noise spectra **b) Noise sources (f = 1,250Hz)**

Fig. 35 Integrated spectra and a sample CLEAN map for "Outboard Wing" regions of Config2. Acoustic map in the right figure obtained from xcoarse simulation.

For most subsonic transports, airframe noise mostly radiates forward. To examine this tendency, integrated noise spectra computed for a flyover directivity angle of 70° are compared to those at overhead (90°) in Fig. 36 with spectral levels adjusted to a common height of 120 m. Note from Fig. 36a that, except for a change in the NLG tone at 450 Hz, the plotted spectra indicate little difference in the combined gear noise at the two directivity angles. However, the Sum of all sources shows measurable differences in noise levels at low and high frequencies, pointing to the directional nature of the noise generated by the high-lift devices. To demonstrate this dependency, noise spectra obtained from the Outboard (OB) Wing regions (shown in Fig. 36b) were used as a representative example. As can be seen in Fig. 36b, the noise produced by the outboard segment of the wing at the overhead position is substantially higher over a broad range of frequencies than that computed for the 70° angle.

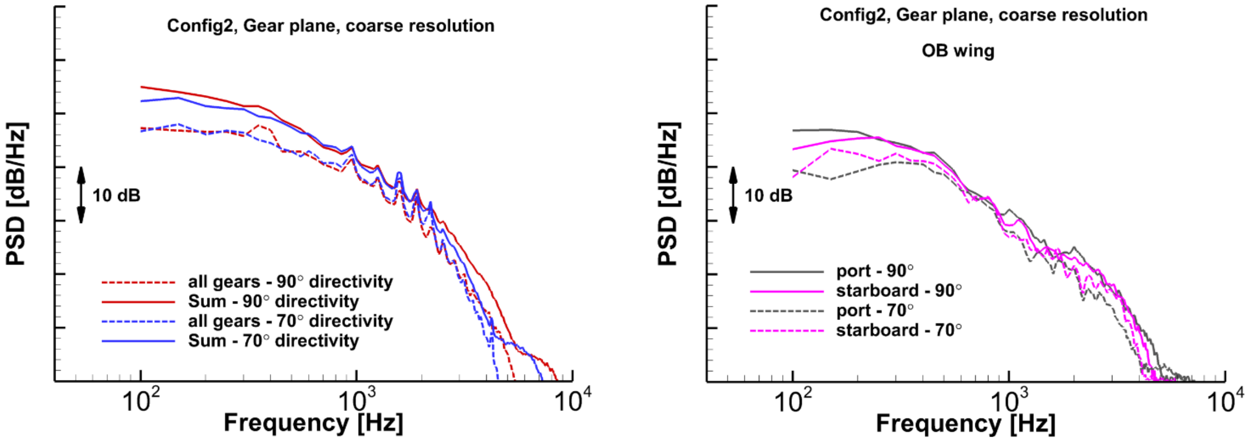

a) All gears and Sum regions **b) Outboard Wing region**

Fig. 36 Forward quadrant far-field noise spectra for Config2, PSD amplitudes adjusted to a height of 120 m.

c. Velocity Scaling for Landing Gear Noise

Simulations for Config1 and Config2 were performed at the speeds listed in Table 1. Thus, velocity scaling laws for the NLG and MLG components cannot be determined directly for either configuration. However, the NLG component is a good candidate for examining the velocity dependencies of the noise spectrum. Data for the two aircraft configurations were used to demonstrate that a) the forward position of the nose gear makes it behave as an isolated source, unaffected by the deflection or retraction of high-lift devices; and b) the NLG follows similar airframe noise velocity scaling trends reported previously for other aircraft. To illustrate the fact that the NLG is exposed to very similar flow fields in both aircraft configurations, the time-averaged velocity fields were sampled at a vertical plane approximately two wheel-diameters upstream of the nose gear axle. Contour plots of the x-component of velocity are shown in Fig. 37. For comparison purposes, the contours have been normalized with the respective freestream speed for each configuration. Except for minor differences, Fig. 37 depicts similar x-velocity fields for Config1 and Config2. The differences can be attributed mostly to the higher AoA of the Config1 simulation. Although not shown, similar agreement was observed for the other velocity components and approaching flow angles in pitch and yaw directions.

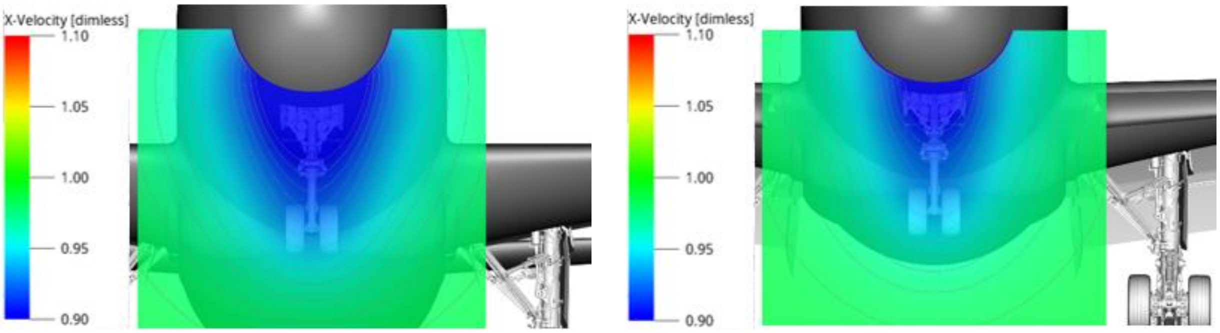

a) Config1 **b) Config2**

Fig. 37 Contours of velocity in x-direction on a vertical plane two wheel-diameters forward of nose gear.

Unscaled NLG far-field spectra for Config1 and Config2, obtained at different speeds, are compared in Fig. 38 with the spectral levels adjusted to a common height of 120 m. For Config2, spectra from both flight test and centered arrays are presented to illustrate the indifference of NLG noise to slight lateral deviations in aircraft position. The flight test measurements of Gulfstream aircraft presented in Refs. [26, 27] clearly indicate a M^6 power law for far-field airframe noise with no Strouhal (St) scaling applied to the frequencies. NLG spectra based on M^5, $M^{5.5}$, M^6, and $M^{6.5}$ scaling without and with St scaling applied are shown in Fig. 39. When no frequency scaling was used, the PSD amplitudes were scaled with the factor $10\log(M_{ref}/M)^k$, where k is the chosen velocity exponent and M_{ref} is the Config2 speed in Table 1. When St scaling was also applied, the PSD levels were adjusted with the factor $10\log(M_{ref}/M)^{k-1}$ and the frequencies were rescaled using the factor (M_{ref}/M). Observe from Fig. 39 that, independent of which velocity exponent was used, applying St scaling does not seem to improve the collapse of the spectral data, reinforcing the trends observed in the flight measurements of Refs. [26, 27]. The best scaling seems to occur with M^6 and $M^{6.5}$, with the former exponent providing marginally better data collapse across the entire frequency range. The excellent collapse obtained for the NLG spectra of Config1 and Config2 confirms our earlier assertion that sources associated with this component are unaffected by the presence of other airframe sources or the deployment of high-lift devices. We also note that the 2.5° difference in AoA between the two aircraft configurations does not seem to affect the NLG far-field noise footprint.

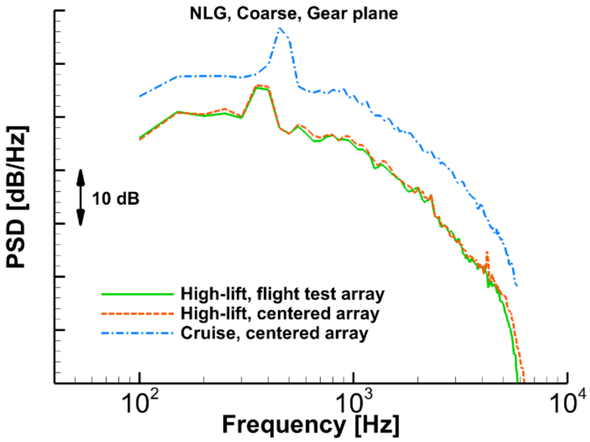

Fig. 38 Unscaled NLG integrated noise spectra from Config1 and Config2.

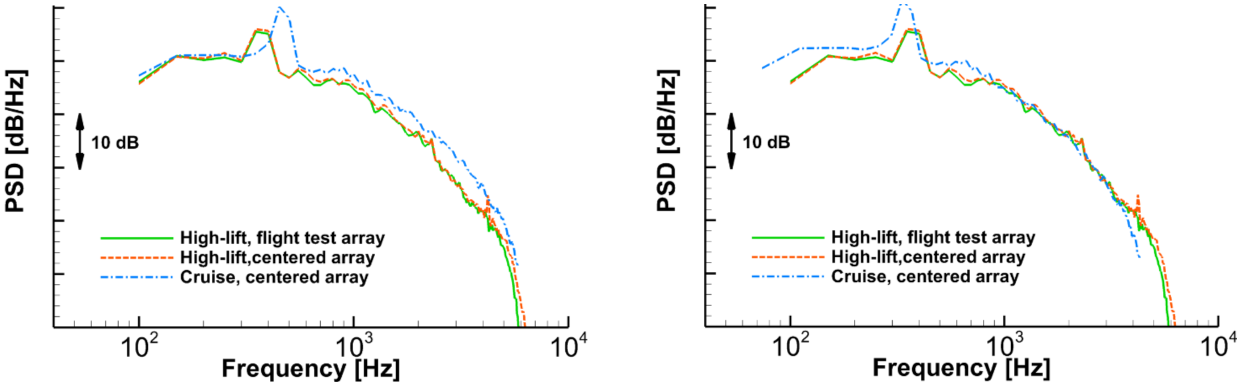

a) M^5 **b) M^5 with St scaling**

Fig. 39 Velocity and frequency scaling applied to NLG integrated far-field noise spectrum; coarse spatial resolution, Gear plane integration.

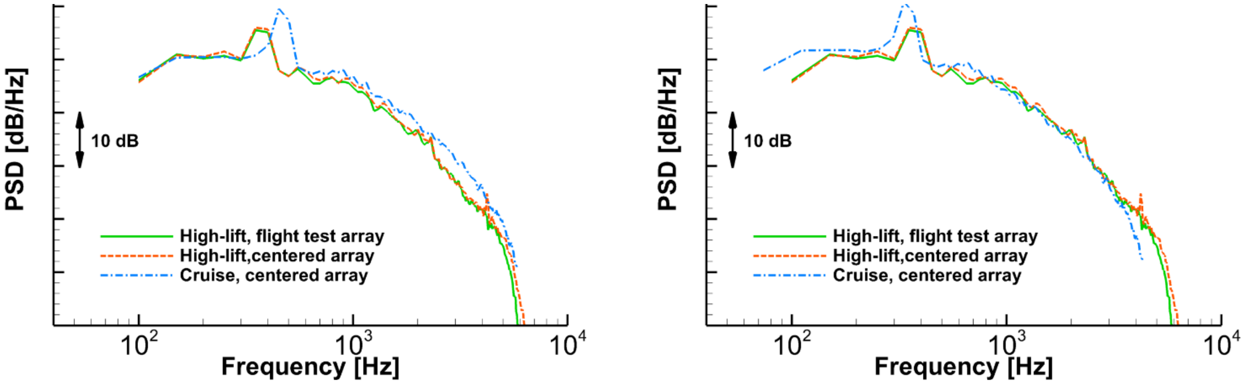

c) $M^{5.5}$ d) $M^{5.5}$ with St scaling

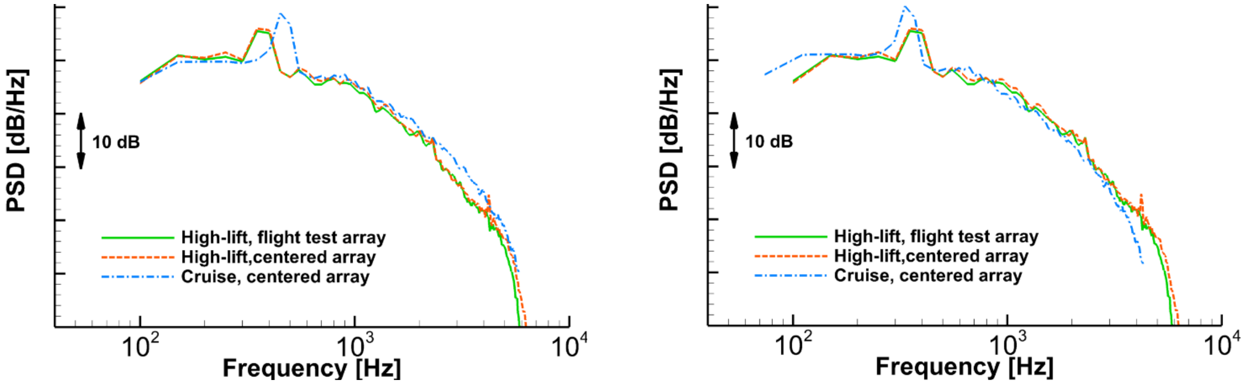

e) M^6 f) M^6 with St scaling

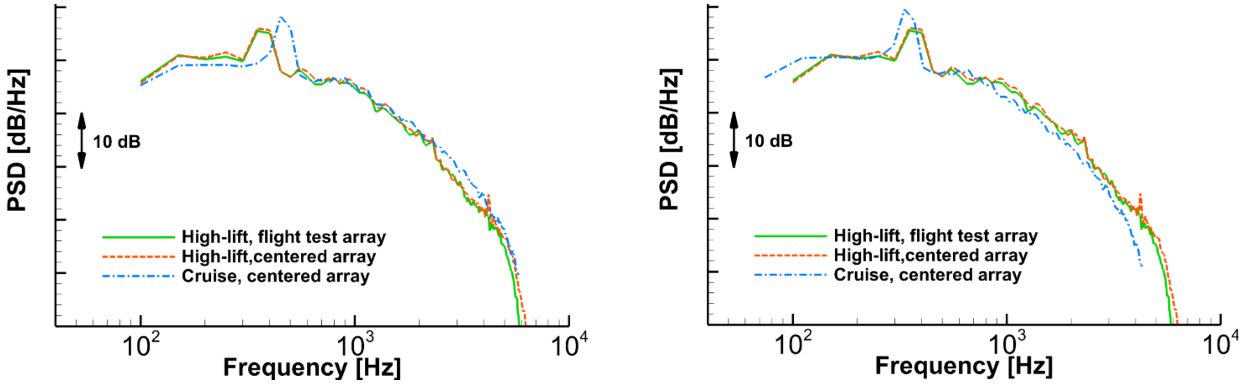

g) $M^{6.5}$ h) $M^{6.5}$ with St scaling

Fig. 39 Concluded.

In contrast to the NLG, there are stark differences between the MLG noise signatures of Config1 and Config2. One clear example is the high-amplitude tones in the MLG spectrum of Config2 that are absent in that of Config1, as shown in Fig. 40 for unscaled spectra normalized to a height of 120 m. Although the substantially higher aircraft speed for Config1 may play a role in the disappearance of these tones, alteration of the local flow approaching the main gear caused by deployment of the high-lift devices is viewed as the more important factor for tonal resonance, as described previously. To highlight the differences in local flow near the MLG, time-averaged x-velocity contours sampled on a vertical plane several wheel diameters forward of the middle axle of the main gear are compared in Fig. 41. As was done for the NLG, the velocities were normalized with the respective freestream speed for each configuration. As evident in Fig. 41, there are substantial differences in the x-component of velocity between the two configurations that cannot be attributed simply to the 2.5° difference in AoA. Although not shown, similarly noticeable differences also exist in the lateral and vertical velocity components that alter the direction of the incoming local flow experienced by the MLG. Note also from Fig. 40 that, although a constant offset in amplitude separates the two sets of spectra at low and moderate frequencies, a noticeably different roll-off is present at frequencies above 1,800 Hz. Scaled spectra based on M^6 without St scaling are presented in Fig. 42a. As can be seen, the spectral collapse is not good. Applying St scaling improves the collapse at lower and moderate frequencies but fails at higher frequencies (Fig. 42b). We emphasize here that grid distribution and spatial resolution surrounding the MLG were identical in the coarse-resolution simulations of Config1 and Config2. Therefore, the dissimilarities in spectral roll-off at higher frequencies cannot be attributed to a lack of resolution or mesh quality in either configuration and are related to the qualitative differences in the local incoming flows experienced by the MLG. Furthermore, the tonal features in the MLG spectra of Config2 partially mask the true magnitude of the broadband component of MLG noise, making the task of determining proper velocity scaling laws much harder.

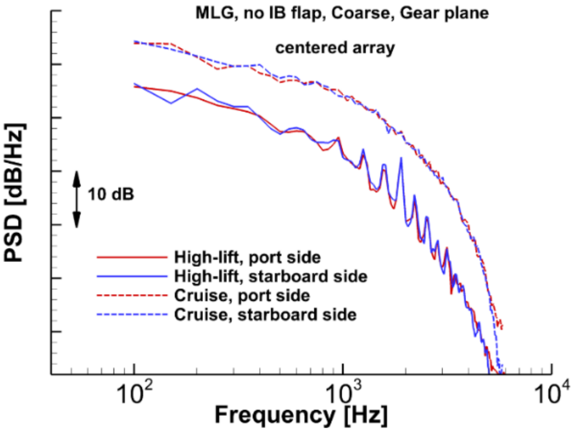

Fig. 40 Unscaled MLG integrated far-field noise spectrum from Config1 and Config2.

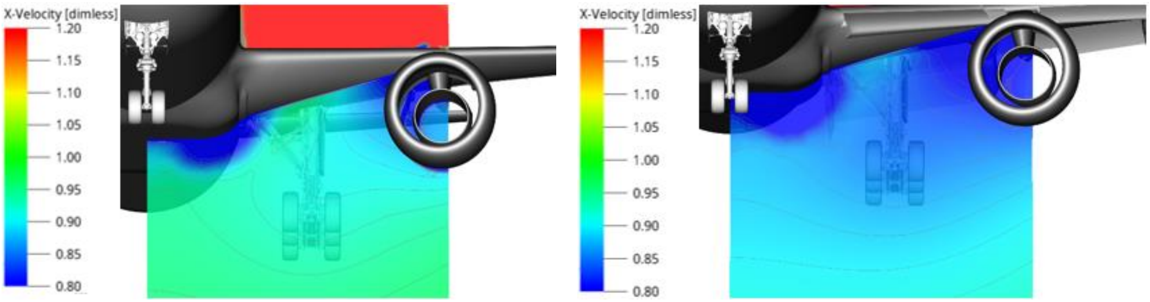

a) Config1 **b) Config2**

Fig. 41 Contours of velocity in x-direction on a vertical plane several wheel diameters forward of main gear.

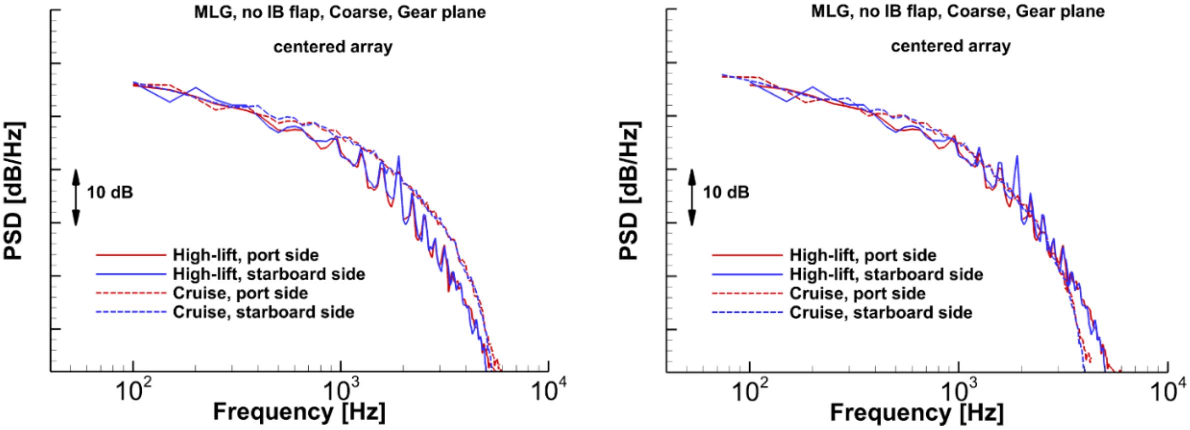

a) M^6 **b) M^6 with St scaling**

Fig. 42 Velocity and frequency scaling applied to MLG integrated far-field noise spectrum.

V. Summary

Aeroacoustic results from a comprehensive computational campaign on airframe noise simulations of a Boeing 777-300ER aircraft in landing configurations were presented. Extreme care was exercised to ensure that the simulated nose and main landing gear are accurate replicas of those currently flown on the aircraft. The full-scale, complete aircraft simulations, executed under a NASA-Boeing collaboration on airframe noise prediction for large civil transports, were the culmination of nearly five years of dedicated work that built upon the experience and knowledge gained from complementary computations for model-scale, isolated and installed B777 main landing gear. The present study, a very successful attempt at simulating the aeroacoustic behavior of a twin-aisle aircraft with an exceptionally high degree of geometric complexity, represents the first step toward fulfilling a grand challenge for airframe noise prediction.

The lattice-Boltzmann flow solver PowerFLOW was used to conduct all simulations. The time-accurate computations were performed for aircraft configurations and conditions executed during the QTD2 airframe noise flight test of the same aircraft. The two chosen configurations were a) landing gear deployed with high-lift devices retracted (Config1) and b) landing gear deployed with high-lift devices deflected (Config2). Both configurations were evaluated without and with a toboggan fairing applied to the main landing gear. All simulations were performed at two spatial resolutions to determine the convergence behavior and accuracy of the predicted aerodynamic forces, CLEAN noise source localization maps, and corresponding integrated spectra. Synthetic far-field pressure records at the QTD2 array microphone locations on the ground were computed via a FWH integral approach with flow quantities on permeable data surfaces as input. The computed array pressure records contained approximately 0.8 s of simulated physical time, providing ample data to achieve statistically meaningful results. The noise signatures of the aircraft undercarriage were determined by integrating the narrowband CLEAN beamform maps on carefully selected integration regions around the components of interest.

For Config1 (high-lift devices retracted), the acoustic maps showed the NLG and MLG to be the dominant noise sources. Integrated far-field spectra confirmed this observation and revealed that the landing gears effectively produced all the noise for this configuration, with no other airframe sources showing up within 10 dB of maximum gear levels. A break-down of the far-field noise indicated that the NLG contributes substantially less than a single MLG over the frequency range that was resolved. For Config1, application of toboggan fairings to the MLG provided a modest amount of noise reduction, on the order of 1–2 dB over the resolved frequency range. To establish a more accurate account of toboggan acoustic performance, simulations at higher spatial resolutions are needed to resolve and capture the noise trends at frequencies above 2,500 Hz.

For Config2, in addition to the NLG and MLG, the acoustic maps showed many prominent sources caused by deflection of wing high-lift devices. For this configuration, integrated far field spectra indicated that the noise generated by the undercarriage was within 3–4 dB of the total aircraft noise, thus comprising nearly half of the total airframe noise. Deflection of the high-lift devices caused a substantial reduction in the noise produced by the MLG relative to NLG levels, a behavior mostly caused by alterations to the local flow field approaching the main gear. In contrast to Config1, NLG sound pressure levels for Config2 were the same, or even slightly higher, than those from a single MLG. Based on a limited assessment of noise directivity in the flyover direction, far-field noise signatures for combined NLG and MLG sources were very similar in the 70° to 90° range. The effects of permeable data surface extent on source strength and location and integrated far-field spectra were studied by comparing results from the nominal surface to those obtained from an expanded surface enclosing a larger volume. Being closer to the aircraft, the nominal permeable surface produced maps that contained spurious sources at frequencies above 2,500 Hz caused by passage of hydrodynamic flow fluctuations through the surface. At a substantial increase in computational cost, we showed that expanding the permeable surface underneath the aircraft eliminated those spurious sources. However, we also demonstrated that, through judicious selection of the integration regions, the integrated spectra obtained from the nominal FWH permeable data surface can be matched exactly to those computed from the expanded surface. Finally, using spectra for the NLG component, we determined that M^6 or $M^{6.5}$ velocity scaling without Strouhal scaling produced the best collapse of Config1 and Config2 levels, confirming the conjecture that the installed NLG can be treated as an isolated source with its noise signature unaffected by deployment of the high-lift devices. The velocity scaling obtained for the NLG agreed with trends obtained from previous flight test measurements of other aircraft.

Acknowledgments

This work was supported by the Flight Demonstrations and Capabilities project under the Integrated Aviation Systems Program of the NASA Aeronautics Research Mission Directorate. We would like to express our sincere appreciation to personnel from the Boeing Company for their assistance in gathering and providing the CAD files of the as-flown B777-300ER nose and main landing gear, in particular Navid Daneshvaran for meticulously resolving some of the MLG geometry questions. The authors also gratefully acknowledge the invaluable contribution of Scott Brynildsen of Craig Technologies for his patience with the tedious task of cleaning and integrating the various aircraft components into a CFD-ready digital representation, as well as providing geometry modifications and CAD support. All simulations were performed on the Pleiades supercomputer at the NASA Advanced Supercomputing (NAS) facility at the Ames Research Center. The logistical support provided by NAS staff in particular is greatly appreciated.

References

[1] Dobrzynski, W., "Almost 40 Years of Airframe Noise Research: What Did We Achieve," *J. Aircraft*, Vol. 47, No. 2, March-April 2010, pp. 353–367.
[2] Chow, L. C., Mau, K., and Remy, H., "Landing Gears and High Lift devices Airframe Noise Research," AIAA Paper 2002-2408, June 2002.
[3] Stoker, R., Guo, Y., Streett, C., and Burnside, N., "Airframe Noise Source Locations of a 777 Aircraft in Flight and Comparisons with Past Model Tests," AIAA Paper 2003-3232, May 2003.
[4] Elkoby, R., Brusniak, L., Stoker, R., Khorrami, M. R., Abeysinghe, A., and Moe, J.W., "Airframe Noise Results from the QTD II Flight Test Program," AIAA Paper 2007-3457, May 2007.
[5] Konig, B., Fares, E. Ravetta, P. A., and Khorrami, M. R., "A Comparative Study of Simulated and Measured Main Landing Gear Noise for Large Civil Transports," AIAA Paper 2017-3013, June 2017.
[6] Ravetta, P. A., Khorrami, M. R., Konig, B., and Fares, E., "Analysis of Simulated and Experimental Noise Sources of the Boeing 777 Main Gear Model via CLEAN in 3D," AIAA Paper 2018-3417, June 2018.
[7] Ravetta, P. A., Khorrami, M. R., Burdisso, R. A., and Wisda, D. M., "Acoustic Measurements of a Large Civil Transport Main Landing Gear Model," AIAA Paper 2016-2901, May-June 2016.
[8] Ffowcs Williams, D. L. and Hawking, J. E., "Sound Generation by Turbulence and Surfaces in Arbitrary Motion," *Philosophical Transactions of the Royal Society of London, Series A, Mathematical and Physical Sciences,* Vol. 264, No. 1151, 1969, pp. 321–342.
[9] Horne, W. C., Burnside, N. J., Soderman, P. T., Jaeger, S. M., Reinero, B. R., James, K. D., and Arledge, T. K., "Aeroacoustic Study of a 26%-scale Semispan Model of Boeing 777 in the NASA Ames 40- by 80-Foot Wind Tunnel," NASA Technical Paper 2004-212802, October 2004.
[10] Storms, B. L., James, K. D., Satran, D., R., Arledge, T. K., Burnside, N. J., Horne, C. W., and Driver, D. M., "Aerodynamics of a 26%-scale Semi-span Model of the Boeing 777 in the NASA Ames 40- by 80-Foot Wind Tunnel," NASA Technical Paper 2005-212829, January 2005.
[11] Horne, W. C., James, K. D., Arledge, T. K., Soderman, P. T., Burnside, N., and Jaeger, S. M., "Measurements of 26%-scale 777 Airframe Noise in the NASA Ames 40- by 80-Foot Wind Tunnel," AIAA Paper 2005-2810, May 2005.
[12] Koenig, B., Fares, E., and Khorrami, M. R., "Aeroacoustic Study of a Subscale Large Civil Transport (STAR) Model – Part 1: Simulations," paper to be presented at the 27th AIAA/CEAS Aeroacoustics Conference in Washington, D. C., June 2021.
[13] Khorrami, M. R., Koenig, B., Fares, E., "Aeroacoustic Study of a Subscale Large Civil Transport (STAR) Model – Part 2: Validation of Simulated Results," paper to be presented at the 27th AIAA/CEAS Aeroacoustics Conference in Washington, D. C., June 2021.
[14] Fares, E., Koenig, B., and Khorrami, M. R., "Effect of Geometric Granularity on the Noise Signature of a Full-Scale Large Civil Transport Nose Landing Gear," paper to be presented at the 27th AIAA/CEAS Aeroacoustics Conference in Washington, D. C., June 2021.
[15] Duda, B., Ferris, R. J., and Khorrami, M. R., "Simulation-Based Assessment of a Full-Scale Installed Quiet Landing Gear," AIAA Paper 2019-2476, May 2019.
[16] Czech, M., Brusniak, L., Khorrami, M. R., Fares, E., and Koenig, B., "Comparison of Boeing 777 Airframe Noise Flight Test Data with Numerical Simulations," paper to be presented at the 27th AIAA/CEAS Aeroacoustics Conference in Washington, D. C., June 2021.
[17] Khorrami, M.R. and Fares, E. "Toward noise certification during design: airframe noise simulations for full-scale, complete aircraft", CEAS Aeronaut J (2019) 10: 31. doi:10.1007/s13272-019-00378-1.
[18] Khorrami, M. R., Ravetta, P. A., Lockard, D. P., Duda, B., and Ferris, R., "Comparison of Measured and Simulated Acoustic Signatures for a Full-Scale Aircraft with and without Airframe Noise Abatement," AIAA Paper 2018-2975, June 2018.
[19] Spalart, P. R., Belyaev, K. V., Shur, M. L., Strelets, M. K., and Travin, A. K., "On the differences in noise predictions based on solid and permeable surface Ffowcs Williams-Hawkings integral solutions," International Journal of Aeroacoustics, Vol. 18(6-7), pp. 621-646, 2019, doi: 10.1177/1475472x19878934.
[20] AVEC Phased Array Software, Version 5.9, AVEC, Inc., Blacksburg, VA, URL: http://www.avec-engineering.com/products.html [cited March 6, 2021].
[21] Khorrami, M. R., Ravetta, P. A., Lockard, D. P., Duda, B., and Ferris, R., "Measured and Simulated Acoustic Signatures of a Full-Scale Aircraft with Airframe Noise Reduction Technology Installed," AIAA Paper 2019-2477, May 2019.
[22] Mueller, T. (ed.), *Aeroacoustic Measurements,* Springer, 2002. ISBN 3-540-41757-5.
[23] Sijtsma, P., "CLEAN based on Spatial Source Coherence," AIAA Paper 2007-3436, May 2007.
[24] Khorrami, M. R., Fares, E., and Casalino, D. "Towards Full Aircraft Airframe Noise Prediction: Lattice Boltzmann Simulations," AIAA paper 2014-2481, June 2014.

[25] Bies, D.A., and Hansen, C.H., *Engineering Noise Control: Theory and Practice,* Spon Press, third edition, 2003. ISBN 0-415-26714-5.

[26] Khorrami, M. R., Lockard, D. P., Humphreys, W. M. Jr., and Ravetta, P. A., "Flight-Test Evaluation of Airframe Noise Mitigation Technologies," AIAA paper 2018-2972, June 2018.

[27] Khorrami, M. R., Lockard, D. P., Humphreys, W. M. Jr., and Ravetta, P. A., "Flight-Test Evaluation of Landing Gear Noise Reduction Technologies," AIAA Paper 2019-2455, May 2019.